NASA CR - 174862

NASA

ADVANCED ION THRUSTER RESEARCH

PREPARED FOR

LEWIS RESEARCH CENTER

NATIONAL AERONAUTICS AND SPACE ADMINISTRATION

Grant NGR-06-002-112

Annual Report

Jan. 1985

Paul J. Wilbur
Department of Mechanical Engineering
Colorado State University
Fort Collins, Colorado

ENTER:

8 1 1 RN/NASA-CR-174862
DISPLAY 09/6/1
85N19021*# ISSUE 10 PAGE 1430 CATEGORY 20 RPT#: NASA-CR-174862 NAS 1.26:174862 CNT#: NGR-06-002-112 85/01/00 63 PAGES UNCLASSIFIED DOCUMENT
UTTL: Advanced ion thruster research TLSP: Annual Report, 1 Oct. 1983 - 1 Nov. 1984
AUTH: A/WILBUR, P. J.
CORP: Colorado State Univ., Fort Collins. CSS: (Dept. of Mechanical Engineering.) AVAIL.NTIS SAP: HC A04/MF A01
MAJS: /*DEFLECTION/*DIVERGENCE/*HOLLOW CATHODES/*ION BEAMS/*ION ENGINES/*ION PROPULSION/*ION SHEATHS/*MAGNETIC FIELDS
MINS: / ANODES/ CATHODES/ ELECTRIC POTENTIAL/ GAS PRESSURE/ NITROGEN/ RING DISCHARGE/ XENON
ABA: Author

1. Report No.	2. Government Accession No.	3. Recipient's Catalog No.
NASA CR 174862		

4. Title and Subtitle	5. Report Date
ADVANCED ION THRUSTER RESEARCH	Jan. 1985
	6. Performing Organization Code

7. Author(s)	8. Performing Organization Report No.
Paul J. Wilbur	
	10. Work Unit No.

9. Performing Organization Name and Address	11. Contract or Grant No.
Department of Mechanical Engineering Colorado State University Fort Collins, Colorado 80523	NGR-06-002-112
	13. Type of Report and Period Covered Annual, Oct. 1, 1983 - Nov. 1, 1984
12. Sponsoring Agency Name and Address National Aeronautics and Space Administration Washington, D.C. 20546	14. Sponsoring Agency Code

15. Supplementary Notes

Grant Monitor - William Kerslake, NASA Lewis Research Center, Cleveland, Ohio 44135.

16. Abstract

A series of experiments conducted on a ring cusp magnetic field ion thruster; in which the anode, cathode and discharge chamber backplate were moved relative to the magnetic cusp; are described. Optimum locations for the anode, cathode and backplate which yield the lowest energy cost per plasma ion and highest extracted ion fraction are identified. The results are discussed in terms of simple physical models. The results of preliminary experiments into the operation of hollow cathodes on nitrogen and xenon over a large pressure range (<0.1 to >100 Torr) are presented. They show that the cathode discharge transfers from the cathode insert to the exterior edge of the orifice plate as the interelectrode pressure is increased. Experimental evidence showing that a new ion extraction grid concept can be used to stabilize the plasma sheath at the screen grid is presented. This concept, identified by the term "constrained sheath optics," is shown to hold ion beamlet divergence and impingement characteristics to stable values as the beamlet current and the net and total accelerating voltages are changed. The current status of a study of beamlet vectoring induced by displacing the accelerator and/or decelerator grids of a three-grid ion extraction system relative to the screen grid is discussed.

17. Key Words (Suggested by Author(s))	18. Distribution Statement
Electrostatic Thruster Hollow Cathode	Unclassified - Unlimited

19. Security Classif. (of this report)	20. Security Classif. (of this page)	21. No. of Pages	22. Price*
Unclassified	Unclassified	64	

* For sale by the National Technical Information Service, Springfield, Virginia 22161

N85-19021#

TABLE OF CONTENTS

Topic	Page
Abstract	i
Ion Thruster Performance Model	1
Ion Beamlet Steering for Two-grid Electrostatic Thruster	2
The Annular Flow Electrothermal Ramjet	3
Ring Cusp Discharge Chamber Studies	5
Apparatus and Procedure	6
Results	14
Effect of Discharge Chamber Length	14
Effect of Cathode Location	19
Effect of Anode Position	23
Conclusions	32
Hollow Cathode Research	34
Apparatus and Procedure	34
Results	36
Conclusions and Recommendations	41
Constrained Sheath Optics	43
Apparatus and Procedure	45
Results	46
Concluding Remarks	48
Three-Grid Beamlet Vectoring	50
Apparatus and Procedure	51
Results	55
Conclusion	55
Appendix A - A Technique for Making Iron Filings Maps in Strong Fields from Permanent Magnets	56
References	57

LIST OF FIGURES

Figure No.	Title	Page
1.	8 cm dia Ring Cusp Thruster with Movable Back Plate	7
2.	8 cm dia Ring Cusp Thruster with Movable Cathode.	8
3.	8 cm dia Ring Cusp Thruster with Movable Anode.	9
4.	8 cm dia Ring Cusp Thruster Magnetic Field Map.	10
5.	Effect of Discharge Chamber Length on 8 cm dia Ring Cusp Thruster Plasma Ion Energy Cost.	15
6.	Effect of Discharge Chamber Length on 8 cm dia Ring Cusp Thruster Extracted Ion Fraction	16
7.	Effect of Discharge Chamber Length on 8 cm dia Ring Cusp Thruster Beam Ion Energy Cost.	18
8.	Effect of Cathode Position on 8 cm dia Ring Cusp Thruster Plasma Ion Energy Cost.	20
9.	Effect of Cathode Position on 8 cm dia Ring Cusp Thruster Extracted Ion Fraction.	22
10.	Effect of Anode Position on Plasma Ion Energy Cost Curve	25
11.	Effect of Discharge Chamber Length on Plasma Ion Energy Cost Curve - Anode Axial Position Optimized.	27
12.	Effect of Anode Diameter on Plasma Ion Energy Cost Curve - Anode Axial Position Optimized.	28
13.	Anode Positions at Points of Discharge Extinction.	30
14.	8 cm dia Ring Cusp Thruster - Effect of Discharge Voltage for Optimized Anode.	31
15.	Hollow Cathode Configurations.	35
16.	Effect of Interelectrode Pressure on Anode Potential.	38
17.	Typical Interelectrode Potential Profiles.	39

LIST OF FIGURES (Continued)

Figure	Title	Page
18.	Qualitative Sheath/Beamlet Behavior.	44
19.	Constrained/Free Sheath Optics Comparison.	47
20.	Three-Grid Deflected Beamlet Nomenclature.	52
21.	Grid Translation Apparatus	53

ION THRUSTER PERFORMANCE MODEL

John R. Brophy

A model describing the performance of high flux density, cusped magnetic field ion thruster designs was developed during this grant period. This work is described in detail in Ref. 1 so it will only be summarized here. The model is formulated in terms of the average energy required to produce an ion in the discharge chamber plasma and the fraction of these ions that are extracted to form the beam. The direct loss of high energy (primary) electrons from the plasma to the anode is shown to have a major effect on thruster performance. The model provides simple algebraic equations enabling one to calculate the beam ion energy cost, the average discharge chamber plasma ion energy cost, the primary electron density, the primary-to-Maxwellian electron density ratio and the Maxwellian electron temperature. Experiments which show the model correctly predicts the variation in plasma ion energy cost for changes in propellant gas (Ar, Kr and Xe), grid transparency to neutral atoms, beam extraction area, discharge voltage, and discharge chamber wall temperature are described in Ref. 1.

The model and experiments indicate that thruster performance may be described in terms of only four thruster configuration dependent parameters and two operating parameters. The model also suggests that improved performance should be exhibited by thruster designs which extract a large fraction of the ions produced in the discharge chamber, which have good primary electron and neutral atom containment and which operate at high propellant flow rates. In addition, it suggests that hollow cathode efficiency becomes increasingly important to the discharge chamber performance as the discharge voltage is reduced. Finally, the utility of the

model in mission analysis calculations is demonstrated. The model makes it easy to determine which changes in thruster design or operating parameters have the greatest effect on the payload fraction and/or mission duration.

ION BEAMLET STEERING FOR TWO-GRID ELECTROSTATIC THRUSTERS

John M. Homa

An experimental study of ion beamlet steering in which the direction of beamlets emitted from a two-grid aperture system is controlled by relative translation of the grids, was completed during the grant period. This work is described in Ref. 2 so it will only be summarized here. The results presented in Ref. 2 can be used to design electrostatic, ion accelerating devices for which the direction and focus of emerging beamlets are important. Deflection and divergence angle data are presented for two-grid systems as a function of the relative lateral displacement of the holes in these grids. At large displacements, accelerator grid impingements become excessive and this determines the maximum allowable displacement and as a result the useful range of beamlet deflection. Beamlet deflection is shown to vary linearly with grid offset angle over this range. Values of deflection-to-offset angle ratio and useful range of deflection are given as functions of grid-hole geometry, normalized perveance level, and accelerating voltage levels. The divergence of the beamlets is found to be unaffected by grid offset over the useful range of beamlet deflection. The grids of a typical dished-grid ion thruster are examined to determine the effects of thermally induced grid distortion and prescribed offset of grid hole centerlines on the characteristics of the emerging beamlets. The results are used to determine the

region on the grid surface where ion beamlet deflections exceed the useful range. Over this region high accelerator grid impingement currents and rapid grid erosion are predicted.

THE ANNULAR FLOW ELECTROTHERMAL RAMJET

Ben D. Shaw

Theoretical analysis of the annular flow, electrothermal, plug ramjet was completed and the results are described in Ref. 3 so the results of this work will also simply be summarized here. In Ref. 3 the ramjet is examined as a possible means of achieving rapid projectile acceleration to velocities for such applications as direct launch of spacebound payloads. The performance of this ramjet device operating with hydrogen propellant is examined for cases where this working fluid is treated (1) as a perfect gas and (2) as a gas that is allowed to dissociate and ionize and then recombine with finite reaction rates in the nozzle. Performance results for these cases are compared to the performance of a conventional ramjet operating with perfect gas, hydrogen propellant. It is shown that the performance of the conventional ramjet is superior to that of the annular flow, electrothermal ramjet. However, it is argued that the mechanical complexities associated with the conventional ramjet would make it impractical, and for this reason the annular flow, electrothermal ramjet is more desirable as a launch system. Models are presented which describe both electrothermal, plug ramjet and conventional ramjet operation, and it is shown that for a given flight velocity there is a rate of heat addition per unit propellant mass for which ramjet operation is optimized. In general, dissociation and ionization losses in the hydrogen propellant are found to be small and nozzle flow is shown to be near

chemical equilibrium rather than the chemically frozen state. It is demonstrated that diffuser shock losses, while significant, do not degrade performance to unacceptably low levels. Data are presented in such a way that they can be used in analyzing various mission profiles. It is demonstrated that the residence times of fluid particles within the electrothermal, plug ramjet are small compared with the times required for flowfield to change significantly. It is argued, therefore, that errors introduced by assuming quasi-steady flow are not excessive. The thermal efficiences over different launch cycles are shown to be high (between 30% and 40%), and the pressure, temperature and power demand requirements are demonstrated to be reasonable.

RING CUSP DISCHARGE CHAMBER STUDIES

Jeff Hiatt

The ring cusp discharge chamber design proposed by Sovey for ion thruster applications in 1982 is attractive because it shows significantly lower beam ion energy costs than its predecessor, the low strength, divergent magnetic field thruster.[4] The reason that the ring cusp thruster shows this improved performance is, however, not clear because several design parameters were changed to transform the low strength, divergent magnetic field thruster into the ring cusp design. Specifically the ring cusp thruster differs from its predecessor, the divergent field thruster, because a) it utilizes high magnetic flux density magnets [a few thousand gauss at the magnet surface vs a few hundred gauss for the divergent field design], b) it effects electron collection at an anode on the magnetic field cusp rather than at an anode between cusps and c) it utilizes a hollow cathode exposed directly to the discharge chamber plasma rather than one that couples through a baffle aperture to the discharge plasma. This last design difference coupled with somewhat different magnetic field shapes for the two designs suggests that primary electrons are supplied to the discharge chamber along different magnetic field surfaces of revolution for the two designs. In order to investigate the effects of changes in magnetic field strength and points of electron emission and collection independently and to determine if still greater performance improvements might be realized in the ring cusp design, a series of experiments were conducted on an 8 cm ring cusp thruster. The thruster used in the study was designed so either the chamber length, the region of electron injection or the anode location relative to the magnetic field cusp could be varied during operation.

Interpretation of the experimental results obtained in this study will be couched in terms of the ion thruster discharge chamber model proposed by

Brophy.[1] By examining the key parameters associated with this model, namely the plasma ion energy cost (ε_p) and the extracted ion fraction (f_B), it will be possible to determine whether improvements in performance caused by changing discharge chamber length, region of electron injection or region of electron collection actually come about because of improved utilization of the energy supplied to discharge chamber electrons, an increase in the fraction of the plasma ion extracted into the ion beam or both.

Apparatus and Procedure

The basic 8 cm diameter discharge chamber used in these studies is shown schematically in Fig. 1. In the configuration of Fig. 1, the chamber is arranged so the steel backplate can be moved axially under the action of the lead screw, yoke and guideposts. In other configurations (Figs. 2 and 3) the lead screw is connected through the yoke and appropriate insulators to either the cathode or anode so their axial location can be varied during operation. In each of these configurations, the steel cylindrical housing has a 9.2 cm inside diameter and both it and the steel backplate are 6.4 mm thick. A single 1.9 cm x 1.3 cm x 0.5 mm thick samarium cobalt magnet on the thruster centerline and a ring of these magnets arranged end-to-end 3.7 cm upstream of the grids drive the magnetic circuit (Figs. 1 and 3). For the cathode study (Fig. 2) the ring magnet is 3.2 cm upstream of the grids. These magnets have a flux density of 0.27 T at their surfaces and they are arranged so the polarity on the outer surface of the ring magnet is opposite to that at the outer surface of the centerline magnet. An iron filings map of the resulting magnetic field for the case where the backplate is 11.7 cm upstream of the grids is shown in Fig. 4. Because of the high magnetic field strengths in this chamber, the unique procedure described in Appendix A had to be developed to make this iron filings map. It is noted that Figs. 1, 2 and 3 show cooling coils on the backplate and sidewalls; they are provided to

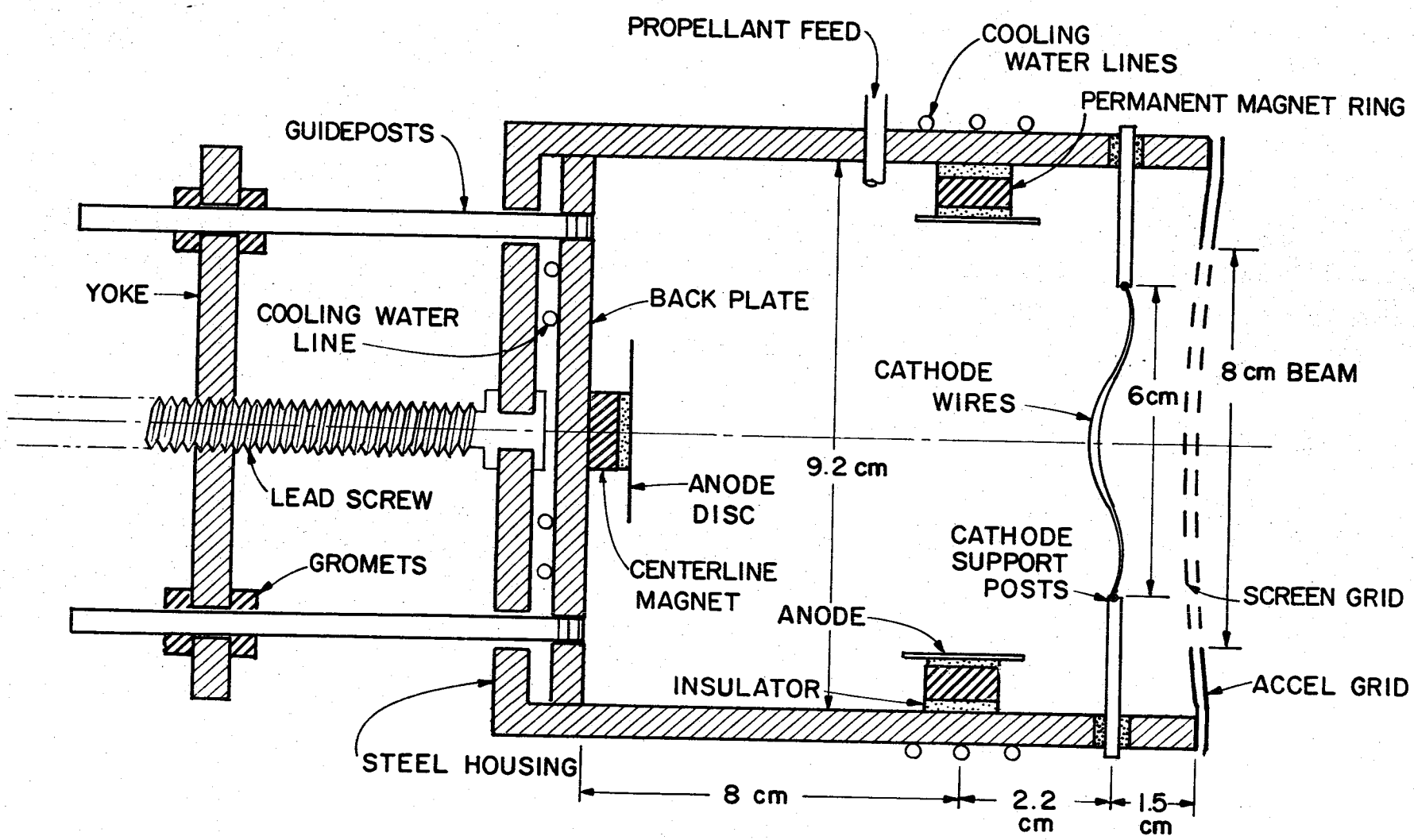

Figure 1. 8 cm dia Ring Cusp Thruster with Movable Back Plate

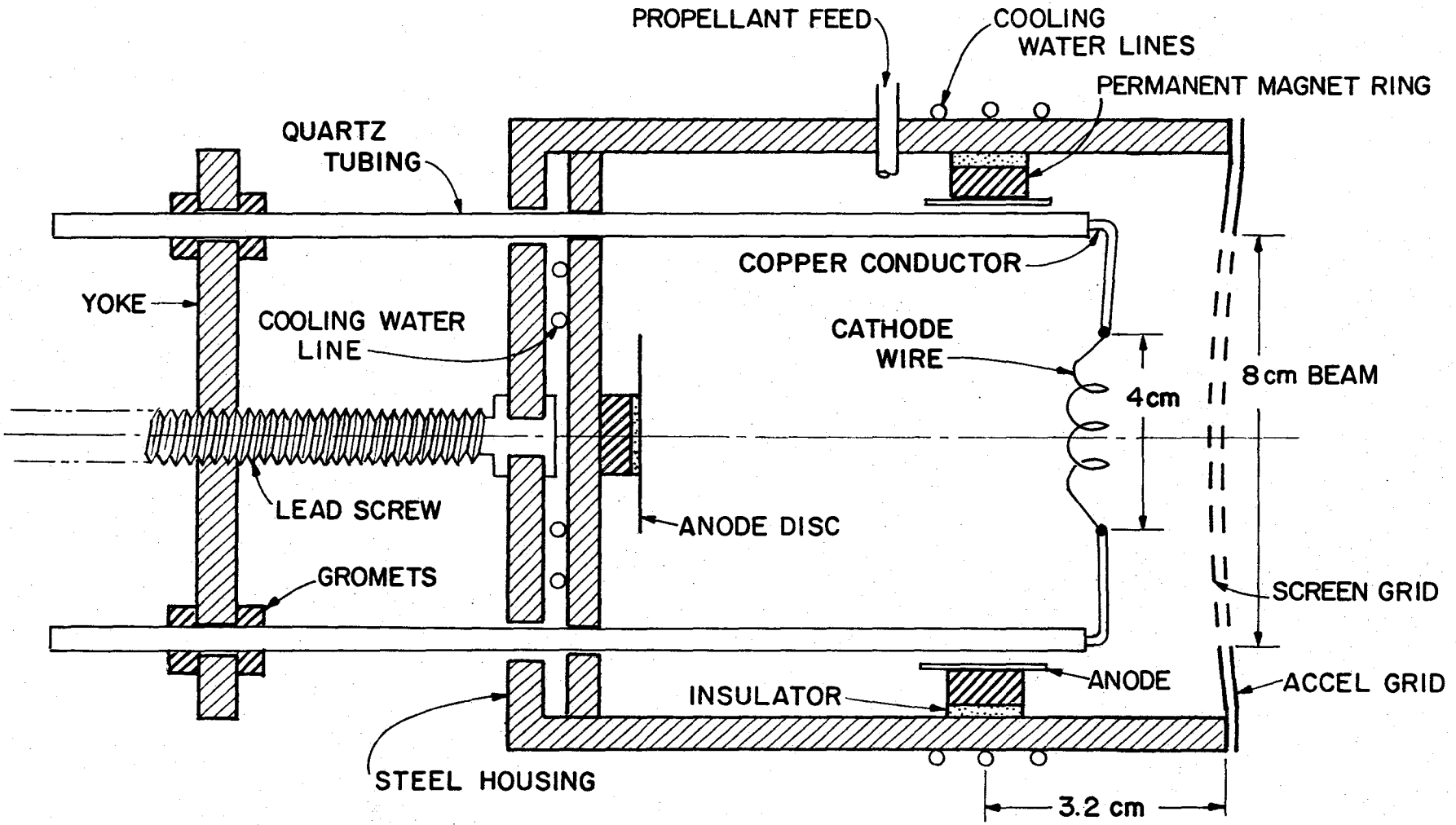

Figure 2. 8 cm dia Ring Cusp Thruster with Movable Cathode

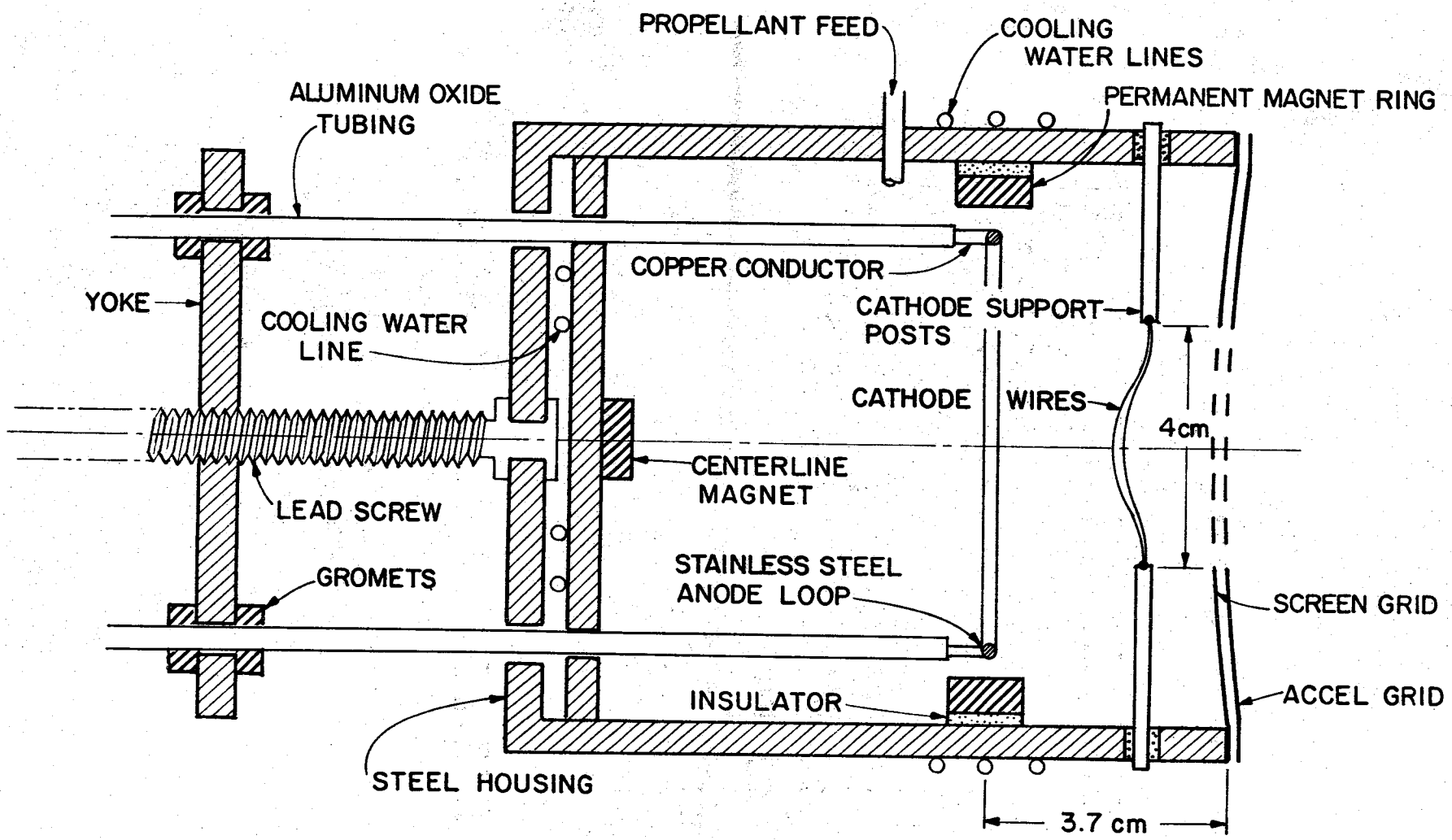

Figure 3. 8 cm dia Ring Cusp Thruster with Movable Anode

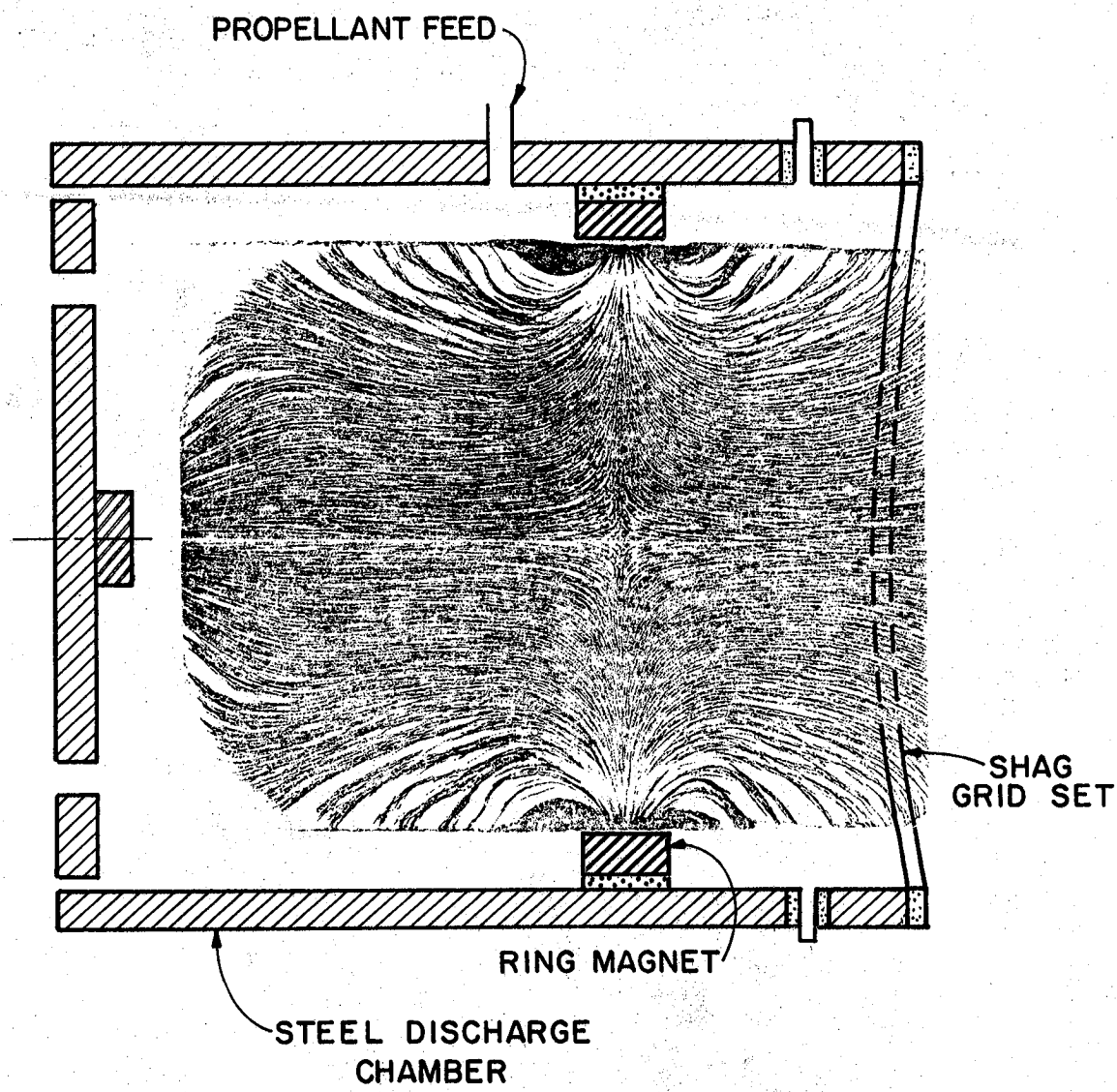

Figure 4. 8 cm dia Ring Cusp Thruster Magnetic Field Map

insure the magnets will not be overheated and to prevent thermally induced binding of the movable backplate.

In all configurations the grids have a cold spacing of 0.86 mm, the screen grid holes are 1.9 mm dia, the accel grid holes are 1.7 mm dia and the hole-to-hole spacing on these grids is 2.2 mm. For all tests the screen grid potential was 750 v, the accel grid voltage was -250 v and argon propellant was fed through the discharge chamber sidewall in the manner suggested in Figs. 1, 2 and 3. The tests were conducted at a discharge voltage of 50 v unless otherwise noted. All tests were conducted in a 45 cm dia vacuum bell jar system in which the background pressure varied over the range 5×10^{-5} Torr to 2×10^{-4} Torr during testing. Neutral densities and propellant utilizations have all been corrected for neutral backflow associated with the bell jar pressure that prevailed during each particular test.

For the discharge chamber length studies, the backplate could be moved over the range from 11.7 cm to 5 cm upstream of the grids during ion source operation. The cold thruster diametrical clearance between the backplate and the cylindrical housing was 0.13 mm. This value was selected as sufficiently great to permit axial motion of the backplate without imposing a large reluctance in the magnetic circuit at the backplate-sidewall interface. For these studies, two 0.25 mm dia tungsten filament cathodes, having a diametrical extent of 6 cm, heated by alternating currents were used. The filaments were located $\sim$ 1.5 cm upstream of the screen grid. The anodes used in this series of tests were 0.25 mm thick steel sheets magnetically attracted toward, but separated from, the centerline and ring magnets by 0.76 mm thick flexible mica sheets--in this configuration electron collection occurs at the magnetic field cusp. For these tests the screen grid was masked down to produce an 8 cm dia. beam.

For the study of the effects of cathode position on performance, the backplate was fixed at an 11.7 cm length and the guideposts of Fig. 1 were replaced by pieces of quartz tubing that housed copper wires supporting a single 0.75 cm dia cathode coil of 0.25 mm dia tungsten wire in the manner suggested by Fig. 2. The coil structure extended 4 cm across the discharge chamber; this configuration was selected to be sufficiently flexible so the wire would not break as it was moved under the action of the lead screw and yoke over its axial range from 0.7 to 7 cm upstream of the grids. Anodes were also located at the magnet surfaces for this study so electron collection occurred at the cusps of these magnets. The screen grid was again masked down to produce an 8 cm dia. beam.

In studying the effects of anode position on performance, the anode position could be varied continuously at each of three backplate axial locations (corresponding to chamber lengths of 11.7, 8.8 and 5.3 cm). The dual, tungsten filament cathode position was however held fixed at 1.5 cm upstream of the grids. In order to conduct these tests, the sheet metal anodes on the magnets were replaced by a single stainless steel wire loop anode supported from the movable yoke by copper wires housed in aluminum oxide tubes after the manner suggested in Fig. 3. Actually anode loops having major diameters of 7.6, 6 and 4 cm were all tested and they could be moved over the range from 1 cm to 10 cm upstream of the grids under the action of the yoke and lead screw. For this test the screen grid was masked to produce a beam diameter of 4 cm.

The basic test procedures used in conducting all of the test were similar and involved establishment of the desired argon mass flow rate ($\dot{m}$) (100-700 mA eq.) and a steady discharge at a 50 v discharge voltage (V_D) and a moderate discharge current (J_D). The discharge current was then changed in increments

and the discharge current, ion beam current (J_B) and ion production current (J_P) were measured at each increment. The parameter of interest (chamber length, cathode or anode location) was then varied and the procedure was repeated. If desired, the propellant flow rate could also be changed and this procedure could be repeated. Extracted ion fractions (f_B) and energy costs per plasma ion (ε_P) were computed from the measured data using the usual equations.[1]

$$f_B = J_B/J_P \tag{1}$$

$$\varepsilon_P = (J_D - J_P)\, V_D/J_P \tag{2}$$

The ion production current was determined in the conventional way[1] for these tests. This is accomplished by biasing the thruster body and screen grid $\sim$ 30 v negative of cathode potential to repel electrons so the ion currents to each of these surfaces can be measured. The sum of the ion currents to these surfaces and into the beam approaches the total ion production current (J_P).* It should be noted that in conducting the study of the effect of anode position on performance the discharge would go out when the anode was moved too far from the axial location of the magnetic field cusp. The axial location of the anode at which this occurred repeatedly for a given anode loop diameter is referred to as the extinction point for that loop. In this report the extinction point will always be the one between the cusp at the ring magnet and the grids because operation of the thruster with the anode on the other side of the cusp (upstream) always resulted in poorer performance.

---

* The error between the true ion production current and the measured current is due to the collection of ions on the anode and the cathode wires and support posts. This error should be small because the areas of these surfaces are small compared to those of the thruster body and grid.[1]

Results

Effect of Discharge Chamber Length

As discharge chamber length increases, the ratio of the path length for a typical primary electron that reaches an anode to its mean free path for inelastic collisions also increases. As a result the probability that a primary electron will lose its energy in an ionizing collision increases. Two recent theoretical models have employed these facts to show the energy cost of a plasma ion should decrease with discharge chamber length.[1,5] Results showing that this trend is also observed experimentally are given in Fig. 5. While these data were obtained at a flow rate of 103 mA eq., this general result was typical over the limited flow rate range investigated. While the data of Fig. 5 suggest this trend is independent of propellant utilization, it should be noted that the theoretical model of the process[1] suggests that the plasma ion energy cost should become independent of chamber length at very low utilizations and high flow rates.

The overall ring cusp thruster performance (beam ion energy cost) is dependent on both on the plasma ion energy cost and the fraction of the plasma ions produced that are extracted into the beam. The typical effect of discharge chamber length on the extracted ion fraction measured in these tests is shown in Fig. 6. It is observed to decrease as the discharge chamber is lengthened, and to decrease less rapidly as the propellant utilization is increased. It should be noted that the curves of Fig. 6 correspond to operation at constant beam current (mass flow rate and utilization are both constant). This leads to the observation that increasing the chamber length causes the extracted ion fraction to decrease because the ion production current increases while the beam current remains constant. The decrease in extracted ion fraction with chamber length is expected because this fraction should be directly proportional

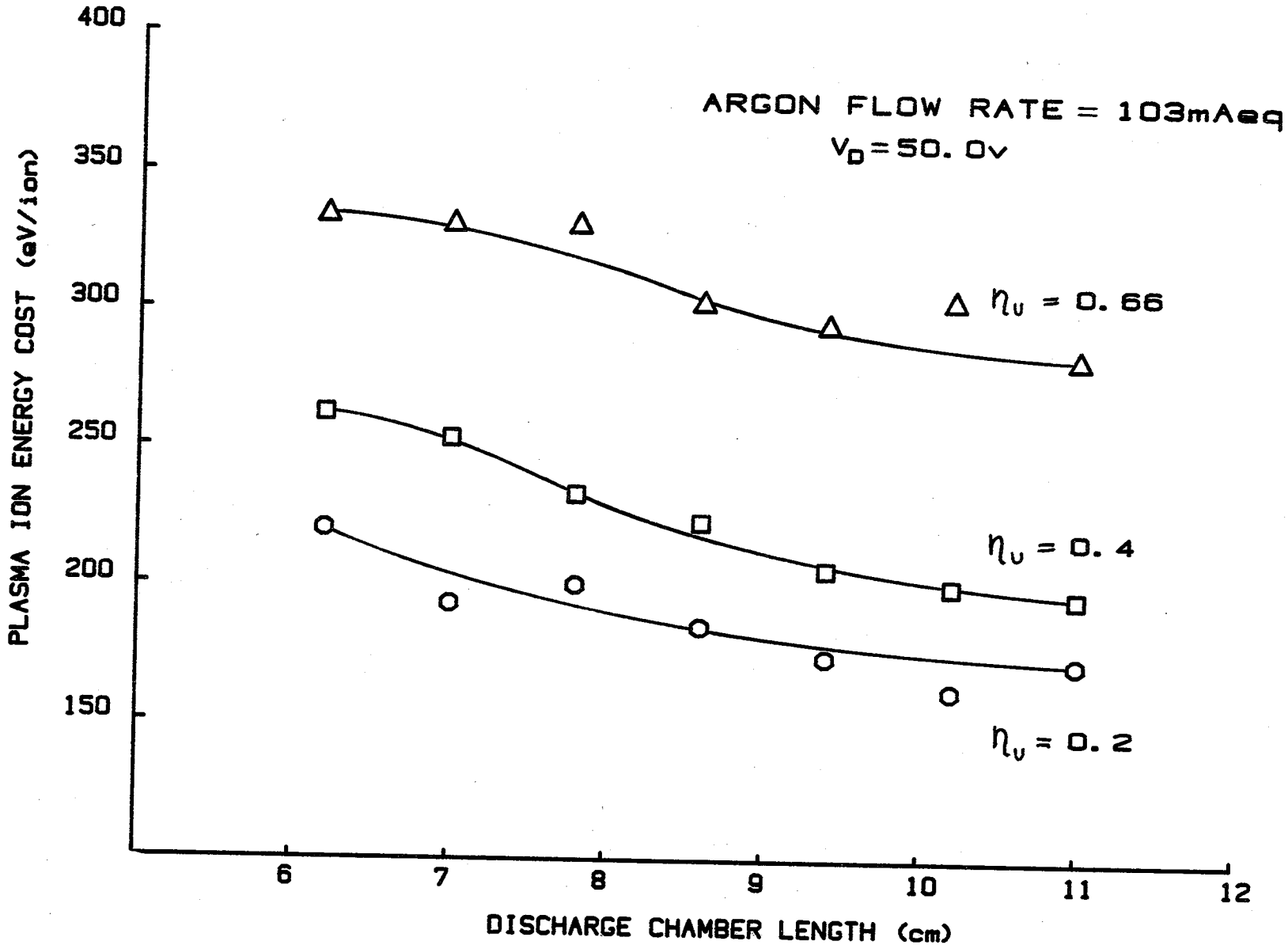

Figure 5. Effect of Discharge Chamber Length on 8 cm dia Ring Cusp Thruster Plasma Ion Energy Cost

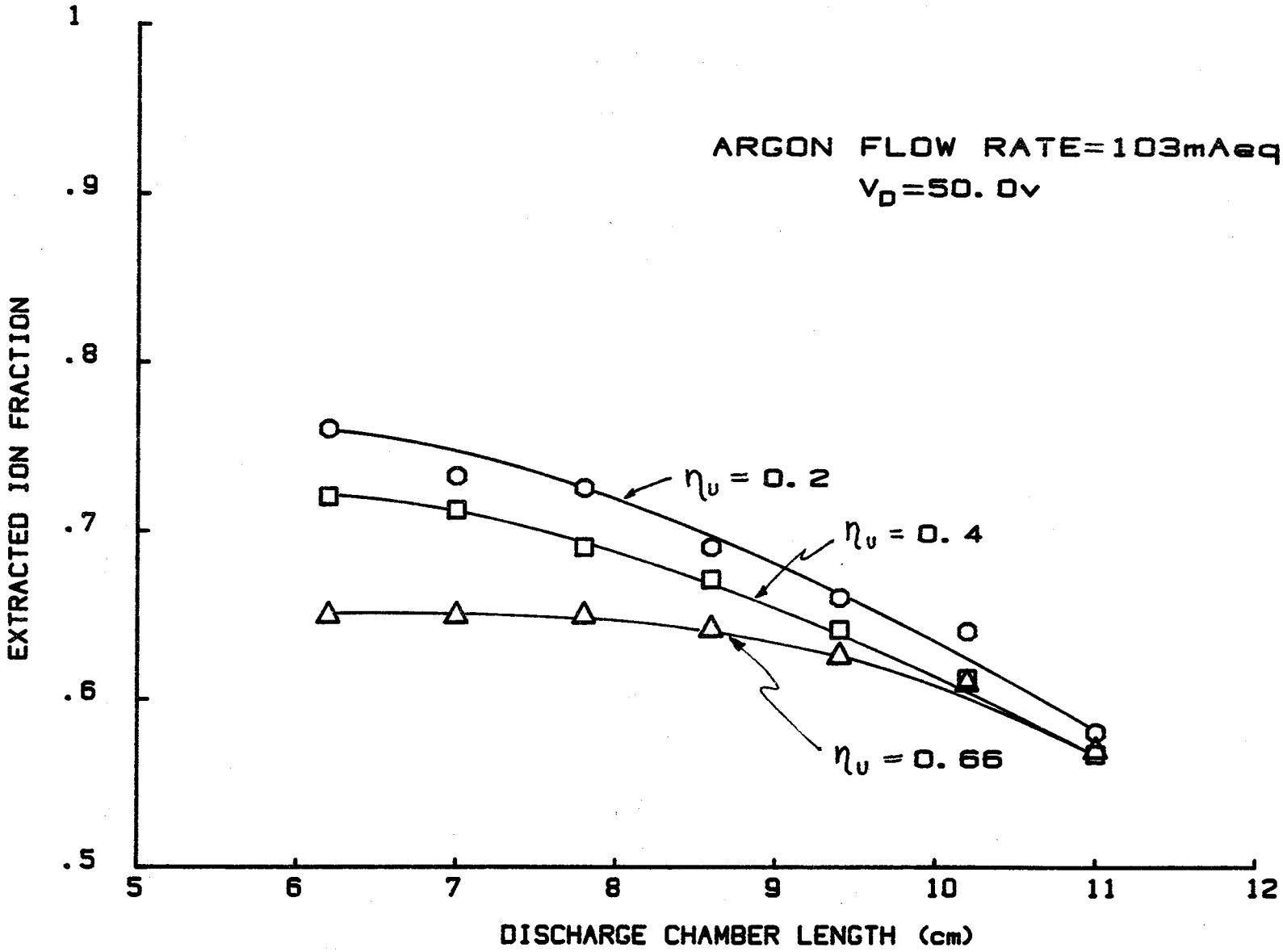

Figure 6. Effect of Discharge Chamber Length on 8 cm dia Ring Cusp Thruster Extracted Ion Fraction

to the ratio of beam cross sectional area to the surface area of the discharge chamber and this ratio decreases with chamber length. The effects of propellant utilization on the extracted ion fraction vs. discharge chamber length curve is not predicted by existing models.

The energy cost of a beam ion (ε_B) is described in terms of the plasma ion energy cost (ε_P) and the extracted ion fraction (f_B) by the equation[1]

$$\varepsilon_B = \frac{\varepsilon_P}{f_B} + \frac{1-f_B}{f_B} V_D \qquad (3)$$

for the present case where the fraction of the thruster interior surface area at anode potential is small. Applying this equation to the results of Figs. 5 and 6 yields the plots shown in Fig. 7. These plots suggest there is an optimum discharge chamber length for this 8 cm dia. ring cusp thruster (i.e. the one of Fig. 1) of 8-9 cm which will yield a minimum beam ion energy cost. This minimum is, however, observed to be quite broad so chamber length does not have a strong influence on performance. It is noted that a similar optimum length was observed by Isaacson and Kaufman for a 15 cm dia. multipole, argon thruster.[6] It is also noted that the results of Fig. 7 apply to the case where electron collection occurs at the magnetic field cusps and the optimum length observed for this case will be shown later to be different from the one obtained when the region of electron collection is moved axially away from the midpoint of these cusps.

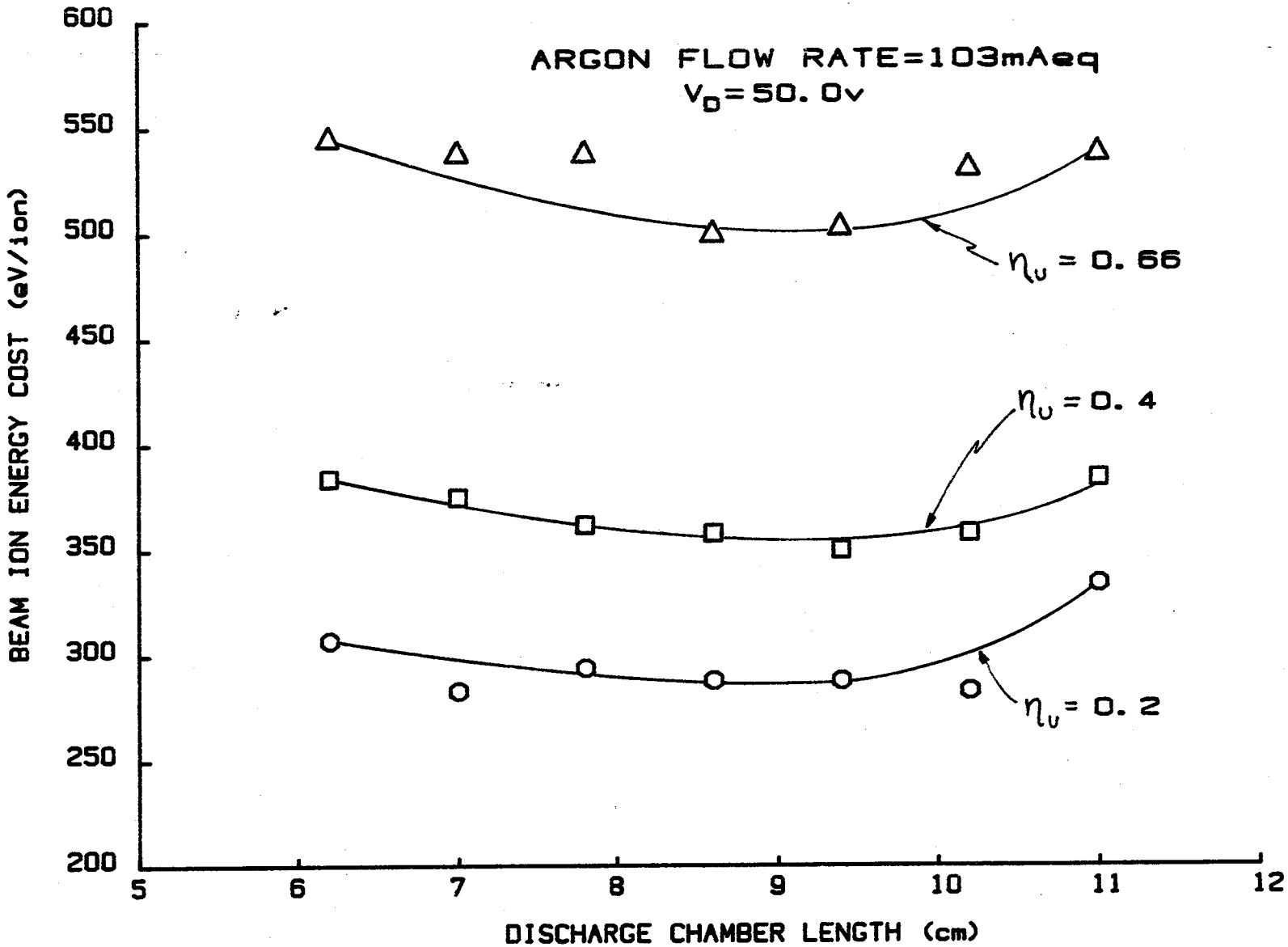

Figure 7. Effect of Discharge Chamber Length on 8 cm dia Ring Cusp Thruster Beam Ion Energy Cost

Effect of Cathode Location

The dramatic effect of the axial location of a filament cathode on the energy cost per plasma ion for an 8 cm dia., 11.7 cm long ring cusp thruster (the one of Fig. 2) is shown in Fig. 8. These particular results were obtained at a propellant utilization (η_u) of 41% and flow rate ($\dot{m}$) of 150 mA eq. but they are typical of all of the results obtained in this study. They show the lowest plasma ion energy cost when the cathode is close to the grids. The plasma ion energy cost is observed to rise rapidly as the cathode is moved upstream from the vicinity of the grids until it peaks as the cathode moves through an axial location near that of the ring magnet and its cusp. Further upstream movement of the cathode causes the plasma ion energy cost to drop slightly and then level out. The horizontal error bars in Fig. 8 indicate the range over which emission occurred from the 0.75 cm dia. spiral cathode wires at a given axial location. It is believed that the highest energy cost per plasma ion occurs in the Fig. 8 data when the cathode is near the cusp because a substantial fraction of the primary electrons emitted from this location can travel in a straight line along the axis of the cusp and its associated converging magnetic field to the anode. This converging magnetic field can be seen in the iron filings map of Fig. 4. When the cathode is moved downstream, toward the grids, direct access to the anode along the axis of the cusp is denied, reflection from the converging magnetic field increases[7] and primary electron losses to the anode decrease. Axial cathode movement into the region upstream of the ring cusp apparently induces the same sort of decrease in losses through the ring cusp but losses to the centerline cusp anode apparently increase and the combined result is that the plasma ion energy cost remains relatively constant. While it may be possible to replace this centerline anode with a cathode potential surface and stop the electron losses to this

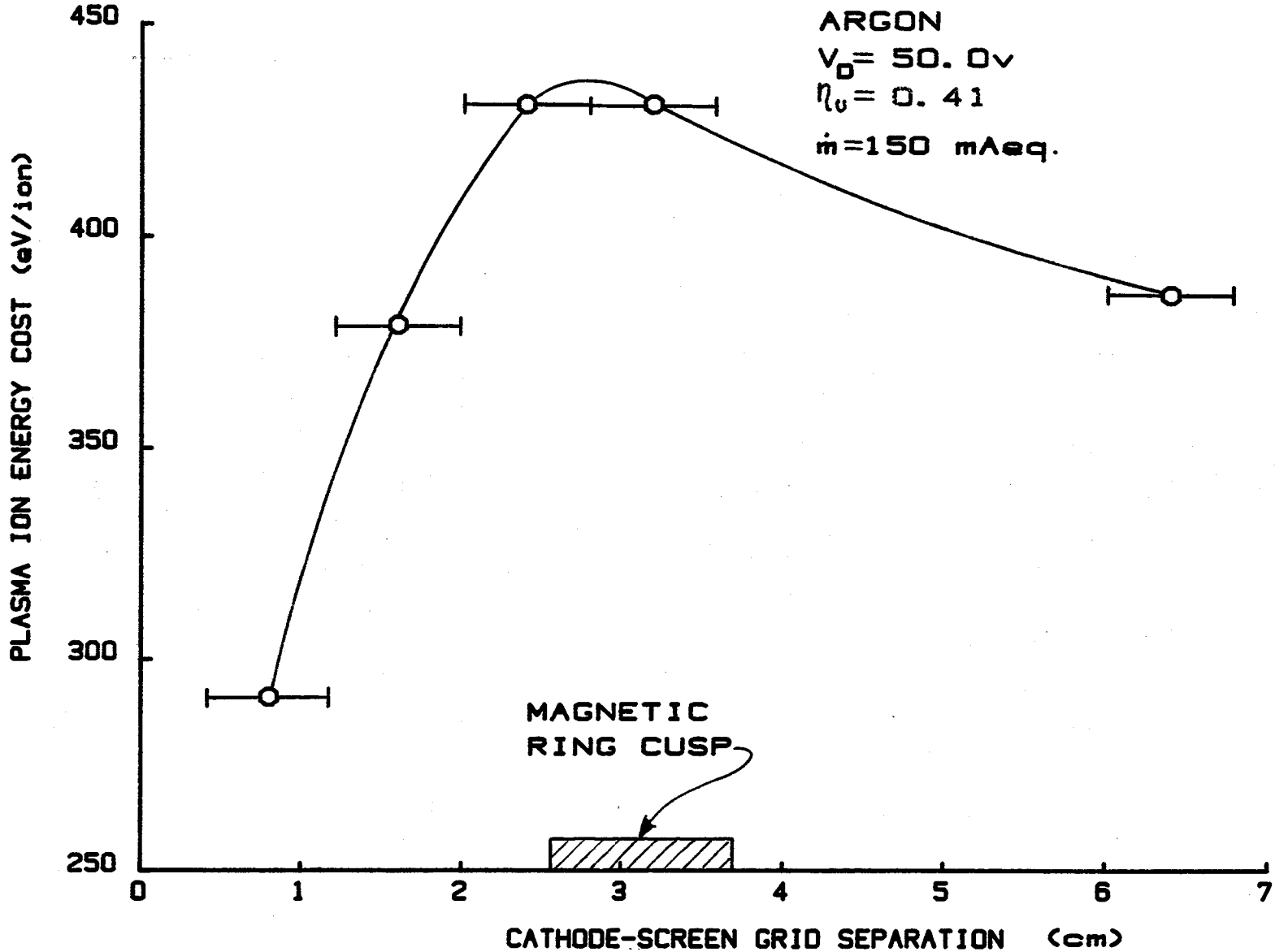

Figure 8. Effect of Cathode Position on 8 cm dia Ring Cusp Thruster Plasma Ion Energy Cost

cusp, this change was not attempted during this study of the effect cathode location on performance.

The percentage of ions extracted from the discharge chamber into the beam was found to decrease as the cathode was moved away from the screen grid toward the magnetic ring cusp. This effect is illustrated in Fig. 9 where the extracted ion fraction is plotted as a function of the cathode-screen grid separation distance. The fraction of ions directed into the beam is seen to reach a minimum when the cathode is near the axial location of the magnetic ring cusp. It is believed that this fraction depends on the diameter of the surface of revolution of the magnetic field line most distant from the thruster centerline at the grids onto which primary electrons are emitted. When the cathode is close to the grids this would be the surface of revolution having the same diametrical extent at the grids as the cathode ($\sim$ 4 cm in the case of Fig. 2). If the cathode were positioned near the cusp, however, Fig. 4 suggests the electrons would be emitted onto field lines that converge as they extend toward the grids. This suggests that in this case the diametrical extent of the primary electron region at the grids would be small ($<<$ 4 cm). It is also postulated that the ion production region corresponds closely to the region occupied by the primary electrons. When the cathode is close to the grids, the ion production region would be large and close to the grids and the extracted ion fraction would, therefore, be high. When the cathode is near the ring cusp, the ion production region is probably small, but more importantly it would be far from the grids and as a result the extracted ion fraction would be small. Although beam profiles were not measured in this study, one would expect the beam profile to be flatter if the cathode were near the grids. It should also be noted that the curve of Fig. 9 is one of constant beam current (flow rate and utilization are both constant). This means that

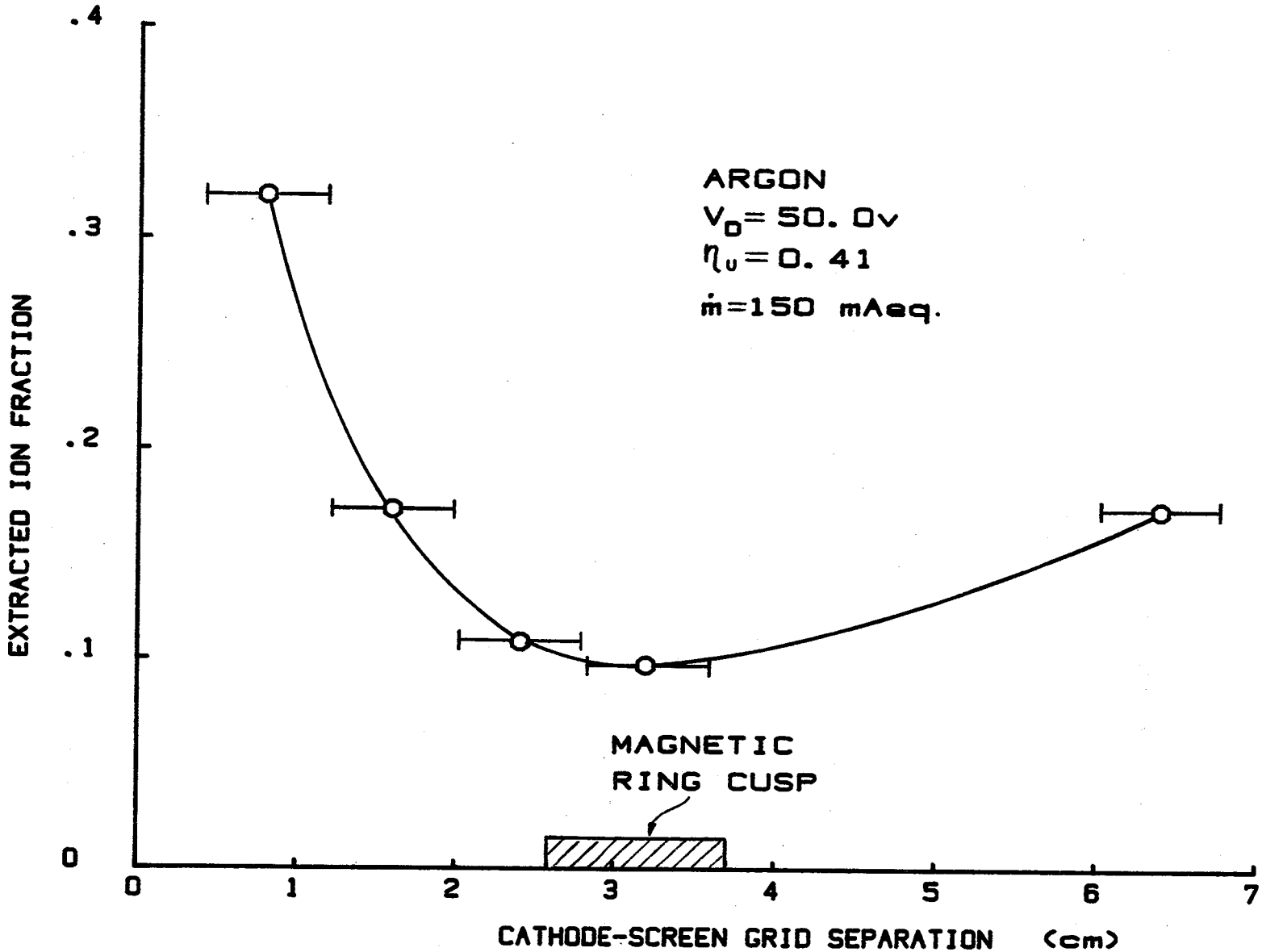

Figure 9. Effect of Cathode Position on 8 cm dia Ring Cusp Thruster Extracted Ion Fraction

operation with the cathode at the cusp implies a higher ion production rate than that realized when the cathode is near the grids.

A phenomenon similar to the one described in the preceeding paragraph was observed when the diametrical extent of the cathode was decreased from 6 cm to 4 cm. This induced a reduction in the general level of extracted ion fraction from the 0.7 range (data of Fig. 6) to the 0.2 range (data of Fig. 9). Again, it is argued that the decrease in the diametrical extent of the cathode induced a reduction in the diametrical extent of the ion production volume near the grids and therefore a lesser ion extraction at the outer radii of the grids.

Figure 9 also shows the extracted ion fraction rising as the cathode is moved upstream of the magnetic ring cusp. This phenomenon can be explained in a similar manner assuming that a small fraction of electrons entering the magnetic cusp region may be reflected onto field lines on the opposite side of the magnetic ring cusp.

Because the plasma ion energy cost decreases and the extracted ion fraction increases as the cathode is moved close to the grids, the best overall performance (lowest beam ion energy cost) is realized with the cathode close to the grids. It should be noted, however, that the discharge becomes unstable when the cathode is too close to the grids. The cause of this instability is not understood.

Effect of Anode Position

When the anode loop shown schematically in Fig. 3 is moved downstream from the axial location of the magnetic field cusp to a point just upstream of the discharge extinction point a dramatic reduction in the plasma ion energy cost is observed. The lowest (optimum) plasma ion energy cost is realized near the threshold of discharge extinction. This effect can be

seen in a plot of the plasma ion energy cost against the parameter $[\dot{m}\ (1-\eta_u)]$, which is proportional to the discharge chamber neutral density. Figure 10 is a typical example of such a plot of data collected over a wide flow rate range in these tests. The extent of the reduction in the plasma ion energy cost induced by moving the anode from the cusp location downstream to that point where extinction is approached (optimized anode location) is seen by comparing the circular and square data symbols. These data can be fitted using the equation proposed by Brophy[1]

$$\varepsilon_p = \varepsilon_p^* \left[1 - e^{-C_o \dot{m}(1-\eta_u)} \right]^{-1} \tag{4}$$

where ε_p^*, the baseline plasma ion energy cost, is the average energy required to produce an ion when losses associated with excitation reactions and Maxwellian electron energy losses to the anode are considered. The primary electron utilization factor, C_o, is given by the equation

$$C_o = \frac{4\ \sigma_o'\ \ell_e}{e v_o\ A_g\ \phi_o} \tag{5}$$

where σ_o' is the total inelastic collision cross section for primary electron-neutral atom collisions, ℓ_e is the primary electron containment length (i.e. the distance primary electrons would travel in the thruster before they would reach the anode if they had no inelastic collisions), e is the electron charge, A_g is the grid area, ϕ_o is the grid transparency to neutral atoms, and v_o is the velocity of the neutral atoms.

The values of the parameters ε_p^* and C_o that resulted in the best fits of the two data sets in Fig. 10 are indicated on the figure. The increase in C_o caused by moving the anode to the optimized location reflects a corresponding improvement in primary electron containment (an increase in ℓ_e). The reason for the decrease in ε_p^* caused by this anode movement is not certain but it is

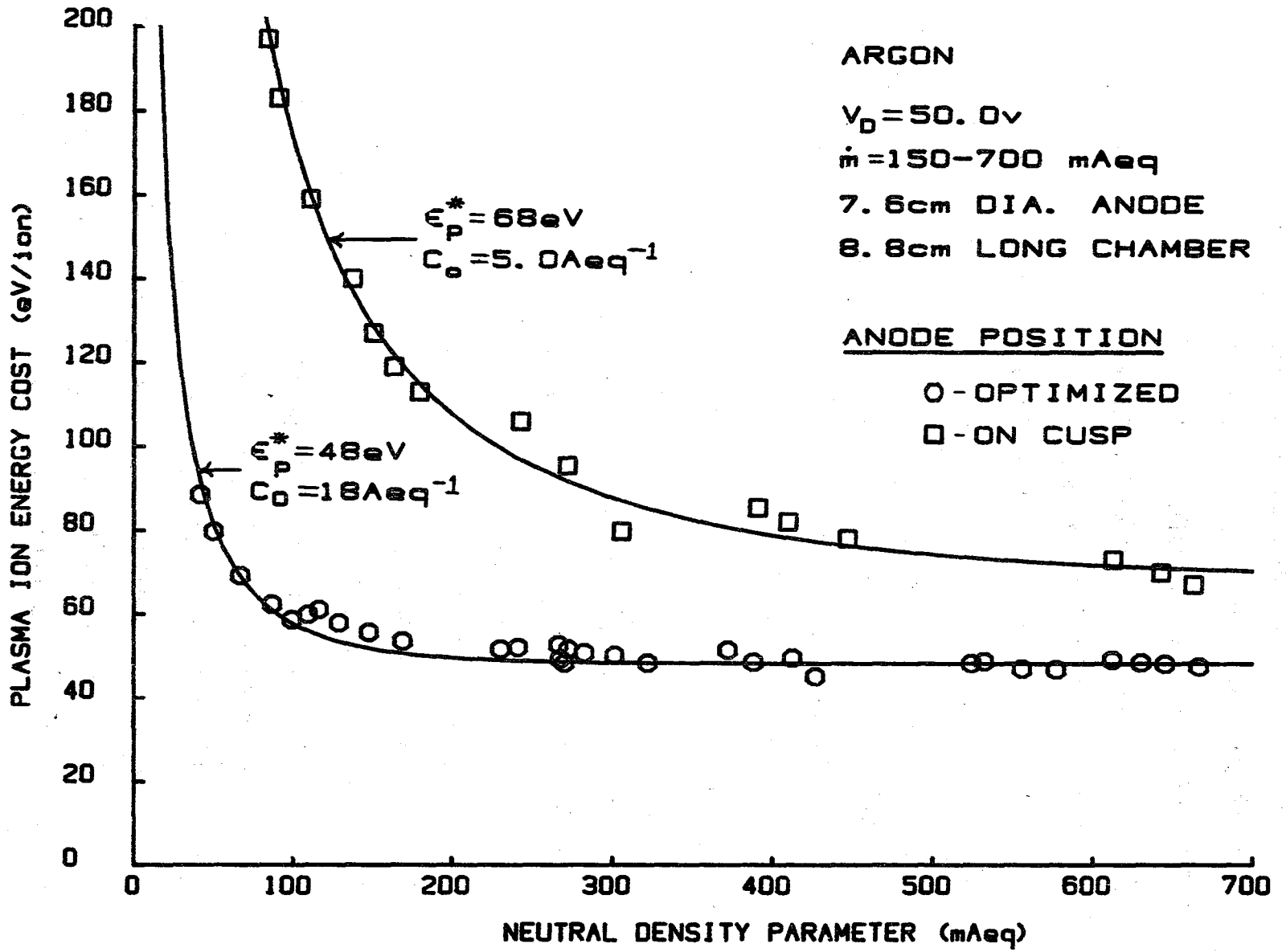

Figure 10. Effect of Anode Position on Plasma Ion Energy Cost Curve

probably due to both reduced ion losses to the anode and reduced Maxwellian temperatures for electrons collected at the anode in the optimized location. When the anode was moved from the cusp location to the optimized location, no significant changes in the extracted ion fractions were observed. Hence the minimum beam ion energy cost is realized when the plasma ion energy cost is a minimum (i.e. at the optimized anode location).

The experimental study of the effect of anode axial position on performance was repeated for three different discharge chamber lengths. Although the axial location of the anode loop at which the performance was optimized changed for each chamber length, the actual level of ion production losses at the optimum performance condition was independent of chamber length. This result is demonstrated in Fig. 11, where plasma ion energy cost/neutral density parameter data for three chamber lengths, are shown to fall on a common curve, characterized by C_o = 17 (A eq.)$^{-1}$ and ε_p^* = 47 eV. This result is important because it implies that by optimizing the anode location relative to the magnet cusp one can define an ion source in which the plasma ion energy cost is independent of discharge chamber length. This leaves the designer free to adjust discharge chamber length to maximize extracted ion fraction.

A study was also conducted to determine how the anode axial position required for optimum performance was affected by changes in anode diameter. With the discharge chamber length held constant, the chamber was operated in three tests, each characterized by an anode loop with a different major diameter. When the anodes were moved near the discharge extinction points in these three tests, the performance was again optimized and the resulting plasma ion energy cost/neutral density parameter data points measured at these anode positions once again fell on a common curve. This curve is shown along with the data points corresponding to each anode diameter in Fig. 12. It is

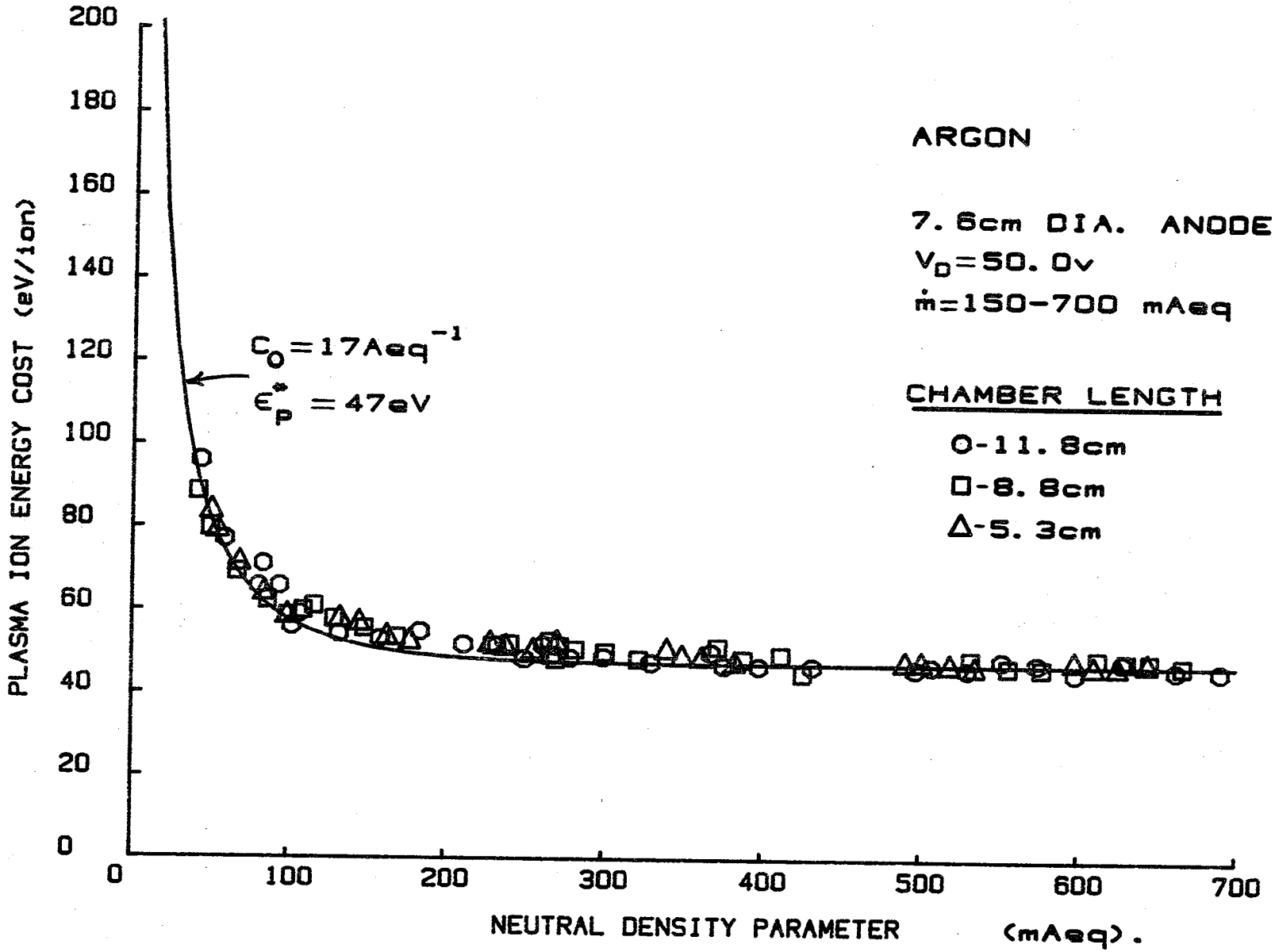

Figure 11. Effect of Discharge Chamber Length on Plasma Ion Energy Cost Curve - Anode Axial Position Optimized

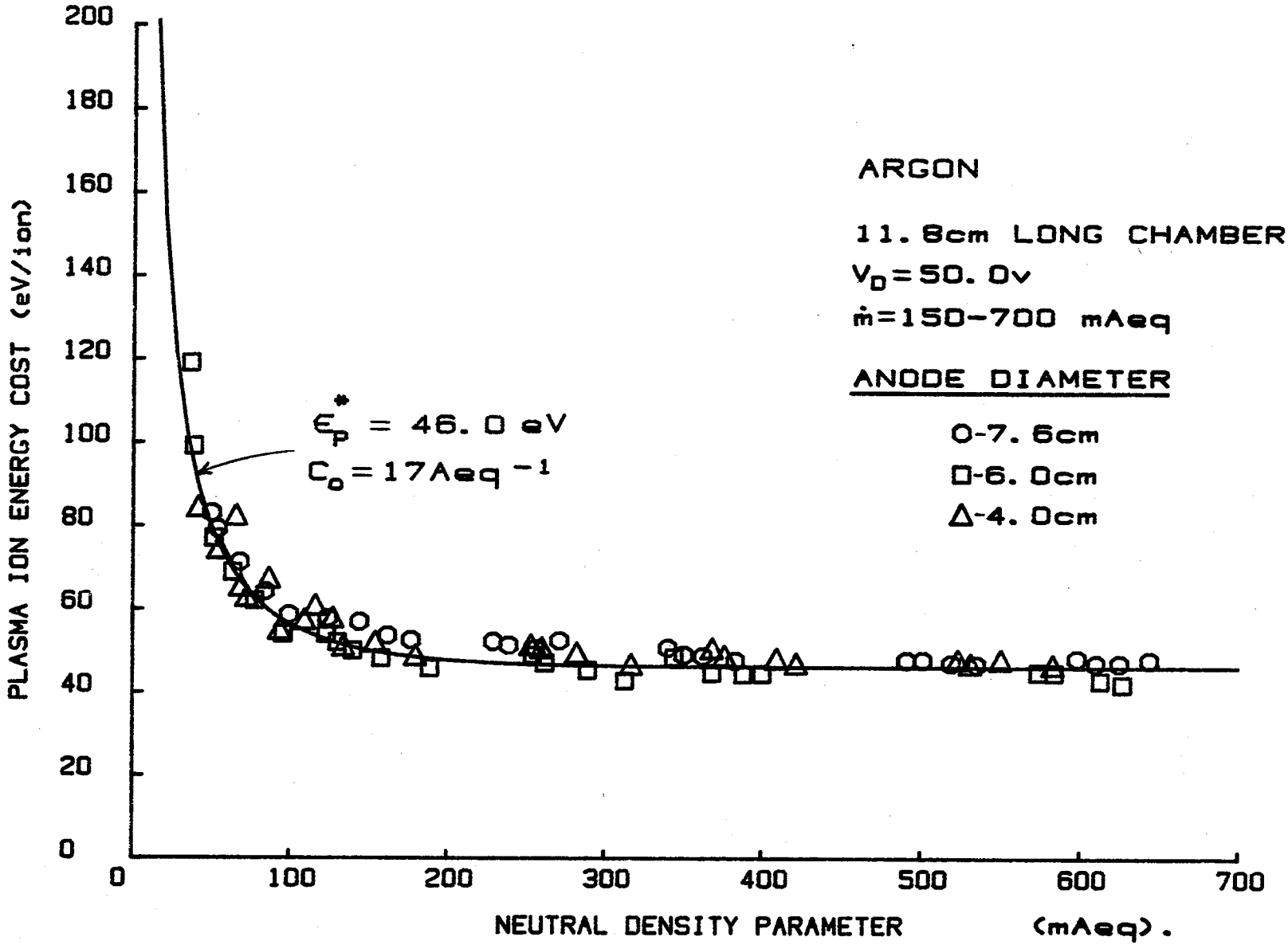

Figure 12. Effect of Anode Diameter on Plasma Ion Energy Cost Curve - Anode Axial Position Optimized

noteworthy that the parameters characterizing the curve of Fig. 12 are essentially the same as those that characterized the curve of Fig. 11. It is noted that the 4 cm anode loop was operated $\sim$ 0.3 cm upstream of the extinction point to prevent excessive discharge current oscillations. These oscillations were not observed with the other anode loops.

The results of Fig. 12 indicate that the same discharge performance characteristics can be achieved with anodes of different diameters if the axial location of each anode is proper. Some insight into which location is proper can be obtained by plotting the optimum anode positions on an iron filings map in the manner shown on Fig. 13. Careful examination of these anode locations suggests that to first order they fall along a single magnetic field line. This in turn suggests that the surface of revolution of this field line serves as a "optimum virtual anode" for collecting electrons. In other words the same performance is achieved in a discharge chamber for an anode positioned to collect electrons at any place along the surface of revolution of a given "virtual anode" field line. It is noted that the distance over which the anode could be moved from the position where the minimum plasma ion energy cost was first achieved to the point of discharge extinction was a function of neutral atom density. At low densities the discharge would extinguished at the same point that the minimum plasma ion energy cost was achieved. As the density was increased it appeared that the anode could be moved through a small distance at the minimum plasma ion energy cost before extinction occurred.

The ion source was also operated at a 32v discharge voltage in the configuration of Fig. 3 with the anode position optimized. The plasma ion energy cost data associated with this test are compared to those at 50v by the square and circular data symbols respectively in Fig. 14. Both sets of data were characterized by baseline plasma ion energy costs (ε_p^*) of 45 eV and by primary

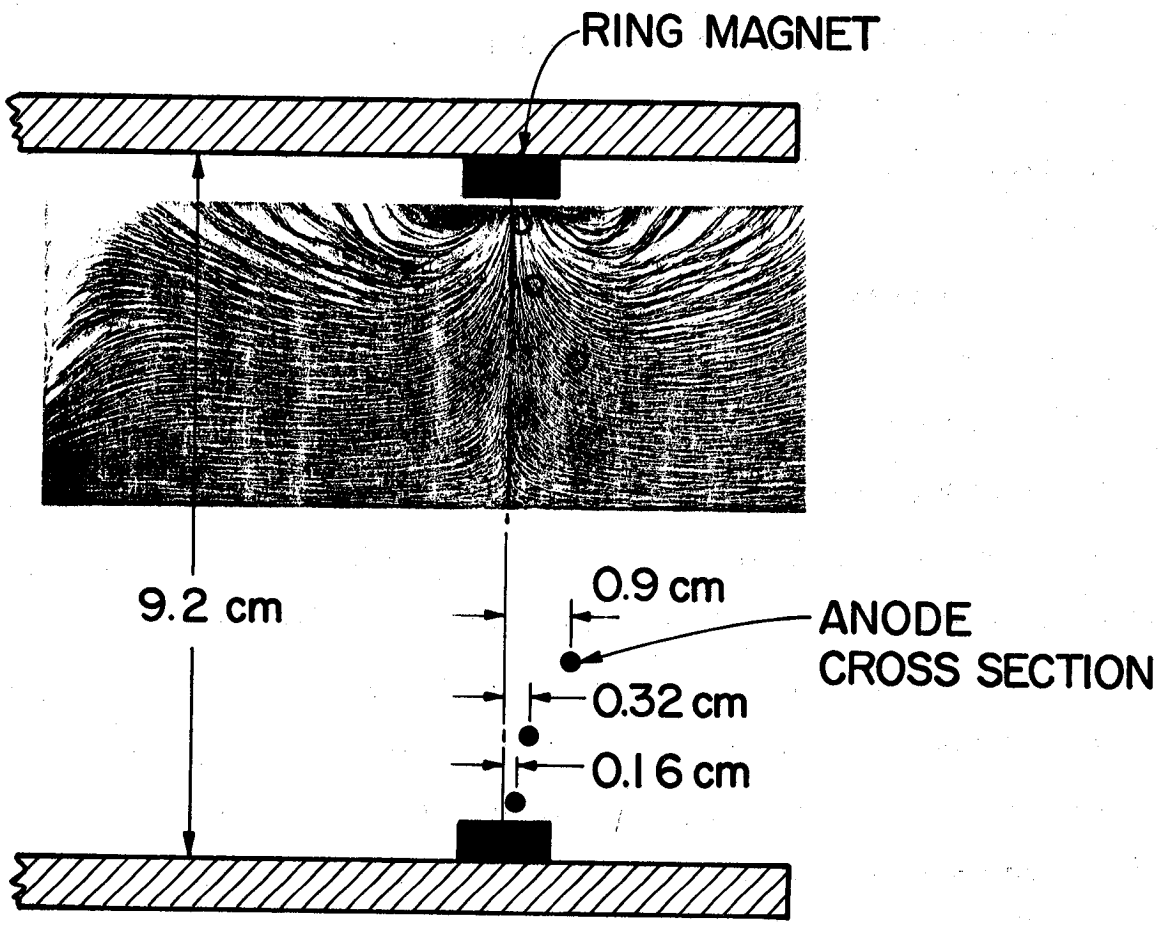

Figure 13. Anode Positions at Points of Discharge Extinction

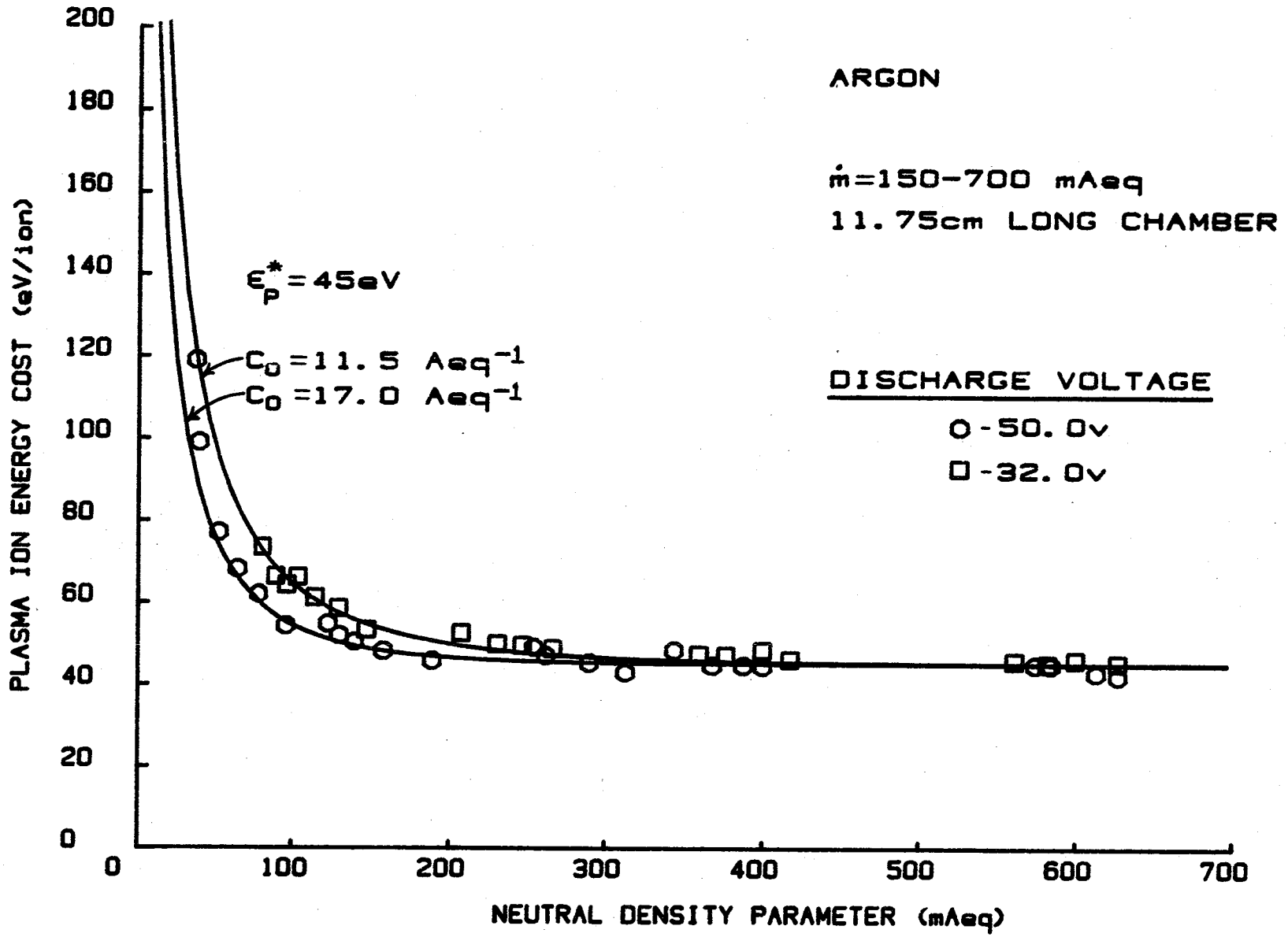

Figure 14. 8 cm dia Ring Cusp Thruster - Effect of Discharge Voltage for Optimized Anode

electron utilization factors (C_0) of 11.5 (A eq.)$^{-1}$ for the 32v discharge and 17 (A eq.)$^{-1}$ for the 50v discharge. Using the 17 (A eq.)$^{-1}$ value for C_0 as a reference value in Eq. 5 with deHeers' collision cross section data[8] one predicts C_0 = 12.8 (A eq.)$^{-1}$ for 32v operation on argon. This value is reasonably close to the value of 11.5 (A eq.)$^{-1}$ determined from the experimental results of Fig. 14. This represents a corroboration of the discharge chamber model for a different discharge chamber diameter than the one Brophy[1] used in his tests.

Conclusions

The most significant finding from this study is probably that the efficiency of an 8 cm dia. chamber having one centerline and one ring magnetic field cusp is improved substantially by moving the electron collection point (anode) from the cusp to a point downstream of the cusp. This finding suggests that the improvement in thruster performance that Sovey[4] achieved with the ring cusp thruster was not due to the fact that he moved the electron collection point from a field line off of the cusp to the cusp itself. Hence the improved performance he observed was caused by either removal of the baffle or the increased magnetic field strength in his thruster. The results of the present study also suggest that the region of electron collection on the anode corresponding to optimum performance may lie at any line of contact on the surface of revolution of the "optimum virtual anode" field line on which incipient discharge extinction occurs. The source of this improvement is a reduction in the plasma ion energy cost for the chamber. Extracted ion fractions do not seem to be affected by the location at which electron collection occurs so long as it is effected in the region between the ring cusp and the grids. Further, the optimum performance level that can be achieved by proper positioning of the anode is the same, regardless of the length of the discharge chamber.

For a ring cusp discharge chamber in which electron collection does occur at the cusps, the length of the discharge chamber and the position of the cathode in the chamber affect both the energy cost of plasma ions and the extracted ion fractions. The most significant beneficial effect associated with these changes can be achieved by placing the cathode close to the grids.

HOLLOW CATHODE RESEARCH

An experimental study of the suitability of hollow cathodes as electron emitters for arc jets was initiated late in the grant period and some preliminary data were collected. The basic philosophy of the study was to begin with a hollow cathode operating in a regime, where it is known to perform well in ion thruster applications, and then extend the operation gradually into the arc jet operating regime, where its performance is not well understood. The transition between these operating regimes has involved changing the propellant from one used in ion sources (xenon) to one suitable for arc jets (nitrogen) and increasing the interelectrode pressure from the ion source regime (of order 0.1 Torr) to that for arc jets (of order 1000 Torr).

Apparatus and Procedure

The basic test configuration used for this study as illustrated in Fig. 15a includes a conventional 6.3 mm dia. orificed hollow cathode and a 5 cm dia. cylindrical, stainless steel, sheet metal anode having its axis concentric with that of the cathode. The hollow cathode, which has a 0.5 mm dia. hole at the center of its thoriated tungsten orifice plate, contains a rolled tantalum foil insert (4 layers of 0.013 mm thick foil) dipped in chemical R-500. The assembly of Fig. 15a is installed in a 30 cm dia. by 45 cm high vacuum chamber that can be isolated from its vacuum pump and back-filled with various gases to $\sim$ 1 atmosphere through a valve connected to the chamber. The interelectrode region can be probed using a Langmuir probe that can be swept from the cathode centerline to the anode surface at any axial location downstream of the cathode orifice plate. The probe has a tantalum electrode that is 0.79 mm dia. by 1.2 mm long. Its output is recorded on an X-Y plotter and analyzed using basically the same procedure as the one developed by Beattie.[9]

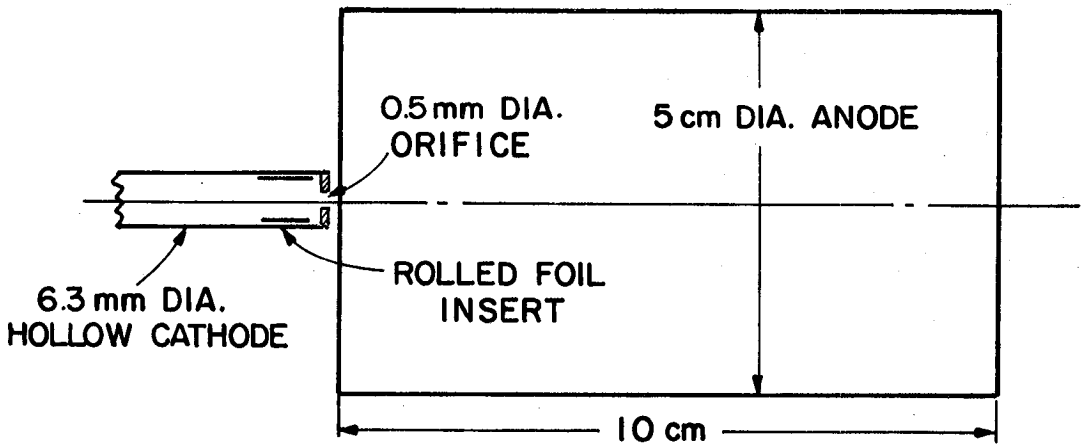

a. TEST CONFIGURATION

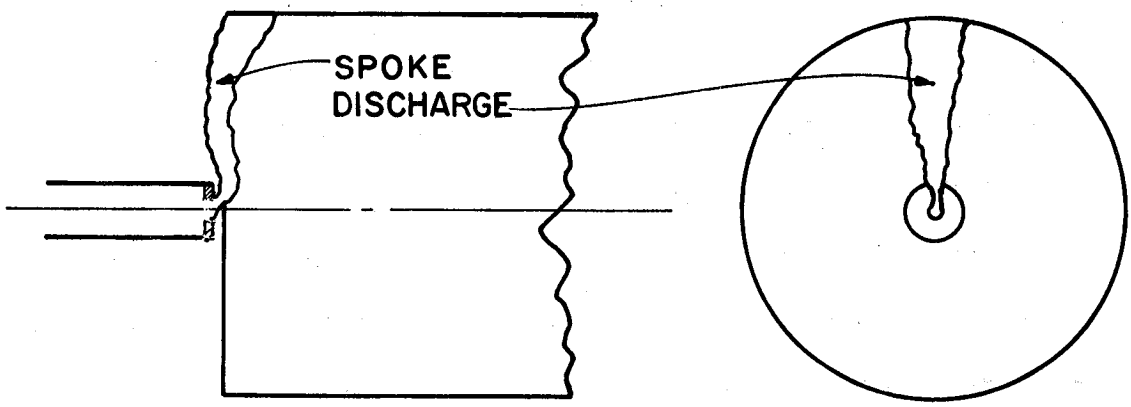

b. SPOKE DISCHARGE FROM INTERNAL CATHODE DISCHARGE

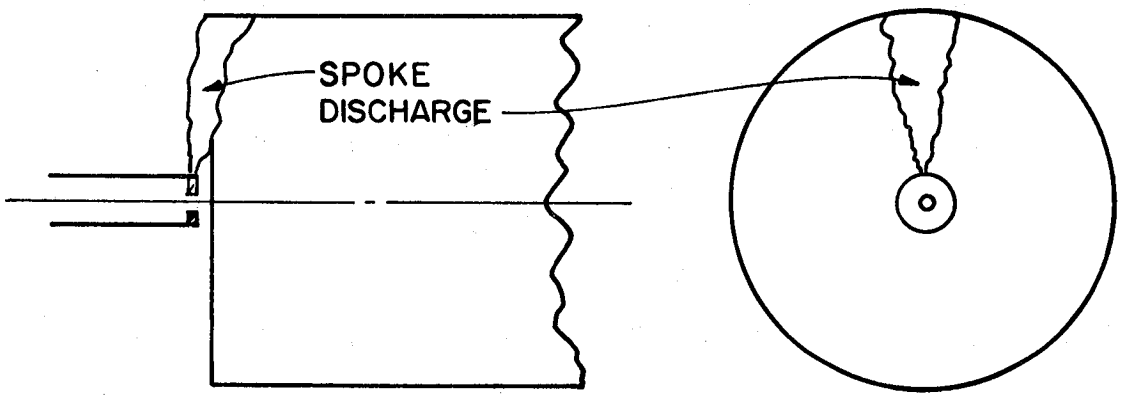

C. SPOKE DISCHARGE FROM EDGE OF CATHODE ORIFICE PLATE

Figure 15. Hollow Cathode Configurations

The test procedure used in this study involved heating the cathode, establishing a flow rate through it ($\sim$ 400 mA eq. for xenon, $\sim$ 5 A eq. for nitrogen) and then applying a few hundred volt potential to the anode until the discharge started and the discharge voltage and heater current could be turned down. During this startup procedure the bell jar pressure was maintained in the range $\sim$ 0.1 - 1 Torr. After startup the cathode flow rate was reduced to 92 mA eq. for xenon or maintained at 5 A eq. for nitrogen and the pressure was maintained in the range $\sim$ 0.01 to $\sim$ 0.1 Torr. The discharge was then allowed to run at 1A discharge current for a few hours to insure operation had stablized. The chamber was then isolated from the vacuum pump and backfilled with the desired gas in increments. After each backfill event the interelectrode pressure was measured using either a Shultz Phelps or mechanical bellows gauge, the anode voltage was noted and Langmuir probe traces were recorded. All tests reported here have been conducted at a 1A discharge current.

Results

When 92 mA of xenon was flowing through the cathode orifice and no backfill was being used the interelectrode pressure was typically $\sim$ 0.01 Torr and the anode voltage required at 1A discharge current was $\sim$ 20v. At this point the discharge luminosity extended from a bright spot at the orifice into a uniform, axially symmetric, rather diffuse plume extending about 3 cm downstream of the cathode. This operating condition is similar to that observed in ion thrusters using hollow cathodes.[10] As the chamber was backfilled with xenon to a pressure in the range of 1 to 10 Torr a luminous sheath became visible at the anode surface and otherwise the appearance of the discharge did not change. In the 10 to 40 Torr range a very luminous spoke passing from the orifice to the edge of the anode in the manner suggested in Fig. 15b

became evident and the luminosity dropped off rapidly away from the spoke. As the interelectrode pressure was increased further no changes in the appearance of the discharge were evident; this discharge continued to pass from the orifice to the edge of the anode. In Fig. 16 a plot of data obtained in a typical run for a xenon-fed, xenon-backfilled cathode shows that the anode voltage remained essentially constant as the pressure was increased over the range from $\sim$ 0.1 Torr to about four orders of magnitude above this value.

Figure 17a shows the potential profile measured through the discharge spoke at the point identified on Fig. 16 by the symbol (1) ($\sim$ 10 Torr). These data suggest a $\sim$ 20v potential rise at the cathode and no additional significant voltage drop either through the spoke plasma or at the anode. Essentially this same potential profile was observed over the complete range of pressures investigated using the xenon-fed cathode and xenon backfill.

When the same xenon-fed hollow cathode was operated in a chamber backfilled with nitrogen the luminous sheath at the anode and the spoke again developed in the same pressure range that they had with xenon. In spite of this similarity the anode voltage required to sustain operation changed dramatically from that for the xenon backfilled one. This difference can be seen by comparing the circular and triangular data points of Fig. 16. Although these data points start out together at low pressure the nitrogen backfill causes the anode voltage to rise with increases in interelectrode pressure. At the point identified by (2) in Fig. 16 the potential profile through the spoke discharge followed the triangular symbols in Fig. 17a. By comparing the data points in this figure one can see the increase in anode voltage induced by an increase in interelectrode nitrogen pressure is required to overcome potential drops at the anode and in the bulk plasma of the spoke. The cathode potential drop is however not affected by the nitrogen backfill pressure so it

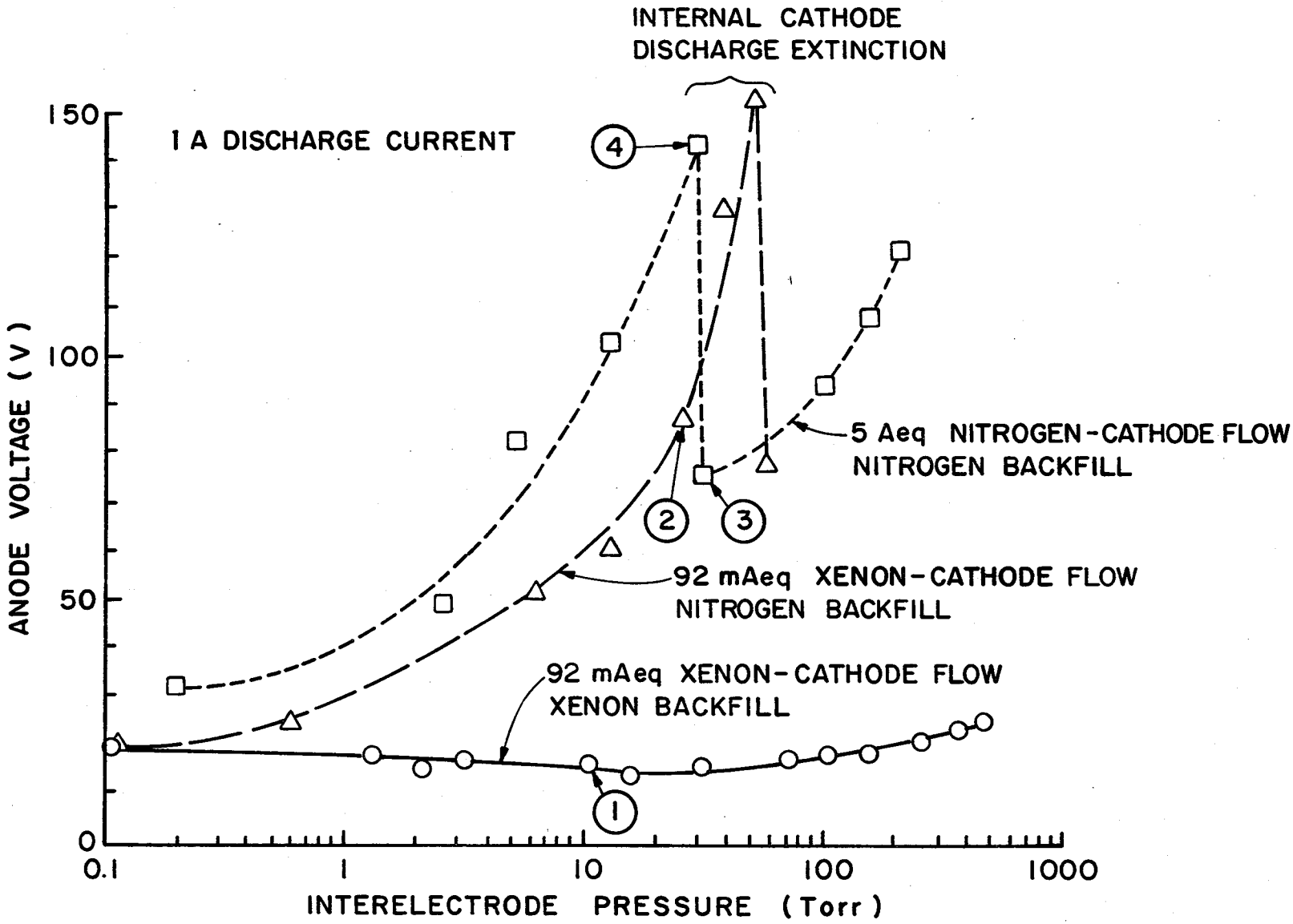

Figure 16. Effect of Interelectrode Pressure on Anode Potential

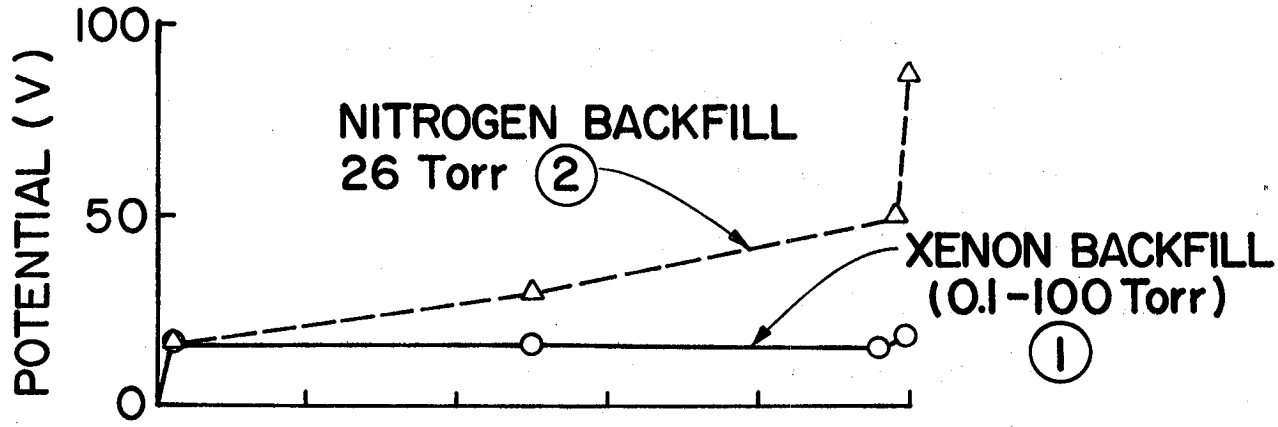

a. XENON-FED CATHODE (92 mA eq.)

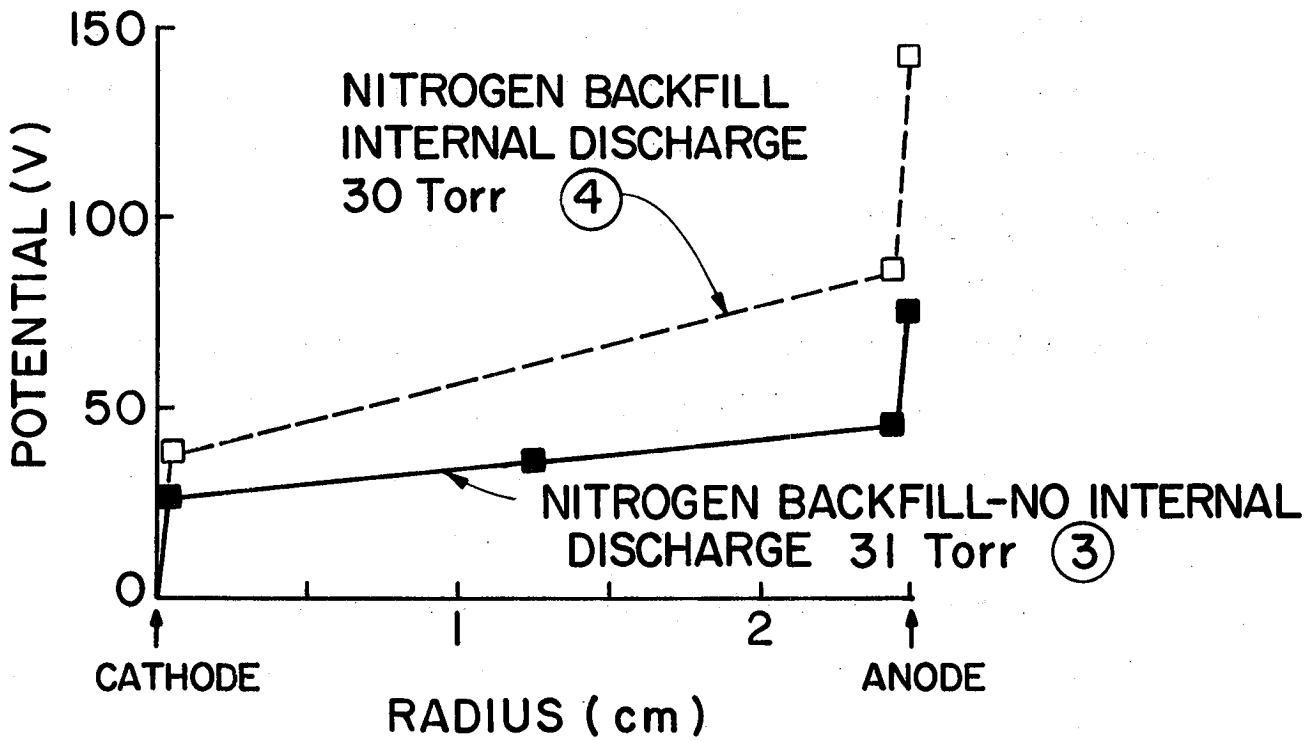

b. NITROGEN-FED CATHODE (5A eq.)

Figure 17. Typical Interelectrode Potential Profiles

appears that the cathode is continuing to operate as it did in the low pressure ion thruster operating regime. It should be noted that an ideal arc jet would have zero voltage drop at the cathode and anode so all of the input power would be going to heat the propellant. Hence the nitrogen-backfilled cathode would be more attractive in this application than the xenon-backfilled one. The spoke observed in both of these tests is, however, undesirable because it implies incomplete heating of the propellant that would be flowing through the interelectrode gap of an arc jet.

As the interelectrode nitrogen pressure of the xenon-fed cathode was increased above about 50 Torr the electron emission site would move from the cathode orifice to the edge of the orifice plate over a time period on the order of a second. As this movement occurs, the anode voltage drops in the manner suggested by the triangular symbols on Fig. 16. It is presumed this occurs because the distance between the electron emission site and the anode decrease when the transition occurs. The discharge generally stabilized with the electron current passing from a very hot spot on the edge of the cathode orifice plate and the upstream edge of the anode (as shown in Fig. 15c). It is noted that the pressure at which this occurred varied from test to test. The general trend was that the pressure that was required to induce the transition in emission sites increased with cathode operating time. Because the work function of the insert generally increases with cathode operating time it is argued that the pressure required to induce the emission site transition from the insert to the edge of the orifice plate increases as the insert is depleted of low work function material.

In a final series of tests the cathode was operated with 5 A eq. of nitrogen flowing through the cathode and nitrogen backfill was used. In this case the discharge behavior was essentially the same as that described for the

xenon-fed, nitrogen-backfilled cathode discharge. The typical anode voltage requirement as a function of interelectrode pressure is shown by the square symbols in Fig. 16. The interelectrode potential profiles for points (3) and (4) on this curve are given in Fig. 17b (solid squares for condition (3) where no internal cathode discharge was present and open squares for condition (4) where an internal discharge was present). The data of Fig. 17b suggest that there is a small cathode voltage drop (in addition to bulk plasma and anode drops) that accompanies increases in interelectrode pressure. This behavior, which was not observed for the xenon-fed cathode, can be seen by comparing the open and solid squares at the cathode location ($\sim$ zero radius). Still the transition of the emission site from inside to outside of the cathode occurred in the same pressure range whether the interelectrode region was backfilled with xenon or nitrogen. It is possible that the cathode voltage drop suggested by the data of Fig. 17b was due in part to the fact that the Langmuir probe was not exactly at the cathode orifice. It had to be located 1-2 mm downstream to the orifice to insure that the probe would not affect the discharge. It is also likely that the nitrogen flow rate could be lowered somewhat to minimize this cathode voltage drop effect. The effects of changes in cathode flow rate have not been investigated at this time.

Conclusions and Recommendations

As the interelectrode nitrogen partial pressure of an orificed, hollow cathode discharge is increased the anode and bulk plasma potential drops increase. The voltage drop at the cathode does not seem to be affected as significantly by this pressure. This leads to the conclusion that most of the energy dissipation in such a discharge occurs at the anode and in the bulk plasma region of the discharge. This in turn suggests that the hollow

cathode should operate as effectively in the high pressure regime of the arc jet as it does in the low pressure one of the ion thruster.

Unfortunately the electron emission site of an orificed hollow cathode moves from inside the cathode to the outside edge of the cathode orifice plate as the interelectrode nitrogen pressure passes through pressures in the range of several tens of Torr. When this transition occurs the anode voltage decreases. In order to prevent this transition the hollow cathode orifice plate could be removed so the discharge can be established normally between the edge of the cathode tube and the anode. It is also noted that one reason for an orifice plate (to maintain the internal pressure in the cathode when external pressures are low) is eliminated when interelectrode pressures are high.

CONSTRAINED SHEATH OPTICS

Both experimental and theoretical studies[11,12] have indicated that the shape of the sheath from which ions are drawn to form ion beamlets in an ion acceleration system, is altered by changes in the discharge plasma properties and the ion extraction voltages. This apparently occurs because altering either the discharge plasma without altering the accelerating voltage or visa versa necessitates a readjustment of the sheath to ensure the Child-Langmuir current density law will continue to be satisfied. For example, decreasing the rate at which ions are supplied to the sheath from a value J_1 to J_2 causes the sheath to move further from the accelerator grid so the space charge limited capacity of the grid system will match and the reduced ion current being supplied. The nature of this sheath motion is suggested in Fig. 18a by the movement from the dashed sheath line (corresponding to J_1) to the solid one (corresponding to J_2). Because the outer boundary of the sheath is constrained by the edge of the screen grid hole, the change in beam current from J_1 to J_2 results in a more concave sheath. This increased concavity in turn causes the qualitative change in the ion beamlet shape suggested by the transition between the dashed and solid beamlet envelope lines in Fig. 18a. If beam current continues to be reduced the ion trajectories begin to cross over each other and excessive direct ion impingement on the accelerator grid occurs.

If on the other hand, the current supplied to the grids is increased the sheath becomes flatter, the beamlet envelope expands and if this trend is continued, direct ion impingement can again become excessive. It is this latter condition that imposes a limit on the ion current that can be extracted at a given accelerating voltage condition. These arguments suggest that one might be able to realize either higher or lower ion beamlet currents at a given accelerating voltage condition without excessive impingement currents if the

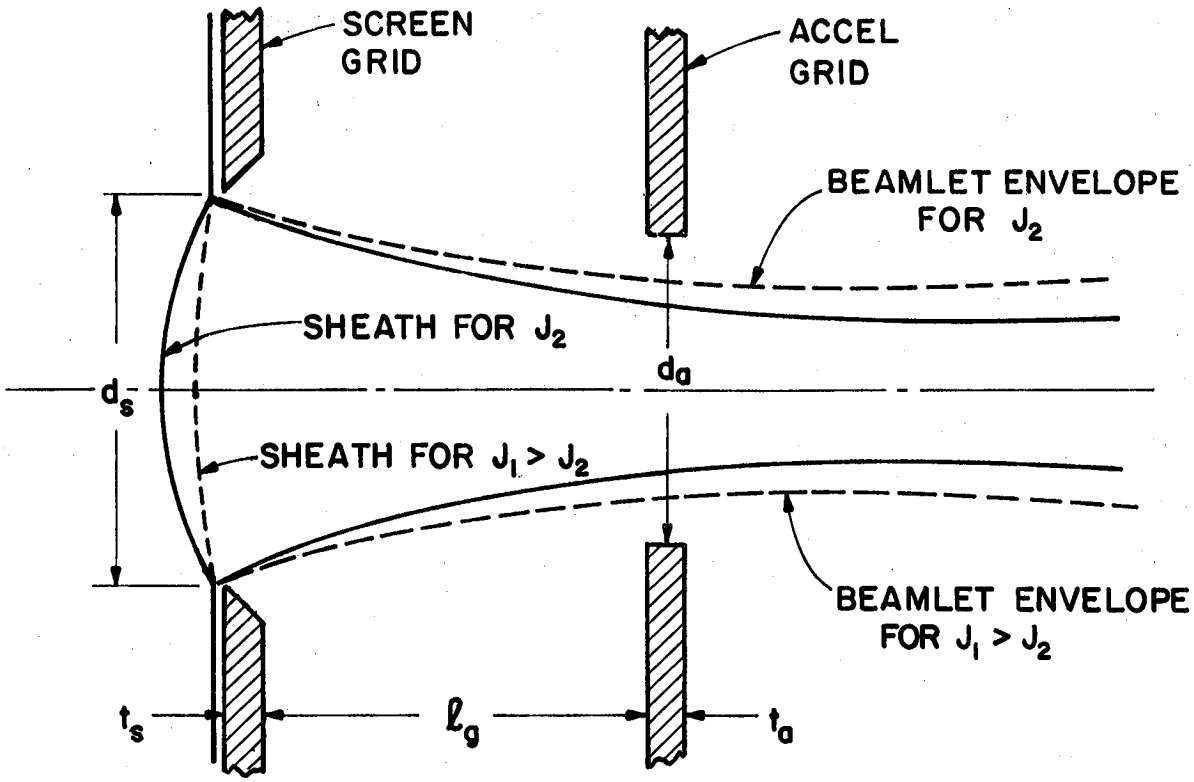

a. FREE SHEATH OPTICS

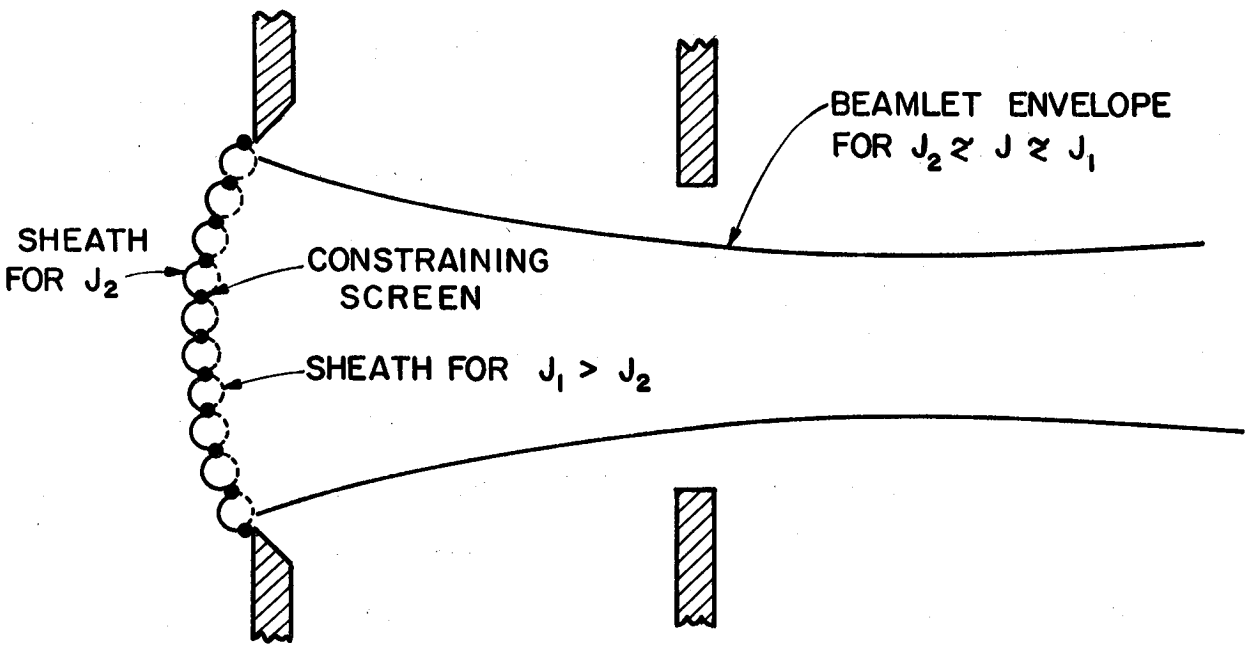

b. CONSTRAINED SHEATH OPTICS

Figure 18. Qualitative Sheath/Beamlet Behavior

shape of the sheath could be controlled.

Several years ago, Byers proposed the use of a fine mesh screen to accomplish the sheath controlling function just described but found that the screen burned through quickly.[13] More recently Aston proposed the decoupled extraction and acceleration concept (DEAC),[14] which includes focusing the screen grids that appear to be serving this same function. The constrained sheath optics system that is the focus of this research involves a screen like the one Byers proposed. The shape of this screen is selected to match the shape of the sheath of a properly focused beamlet.[11] The basic concept of constrained sheath optics is then to place a constraining screen on the screen grid hole that would induce many sheaths that would move in the manner suggested in Fig. 18b as the beam current was changed from a high value J_1 to a lower one J_2. Because the overall sheath is constrained to the basic concave shape shown in Fig. 18b, it is argued that the beamlet envelope remains relatively unchanged as these beam current changes are introduced.

Apparatus and Procedure

In order to test the validity of this concept, a special 8 cm dia. ring cusp ion source designed for ion implantation applications and equipped with a single 2.9 cm dia. screen grid aperture was modified to serve as a test bed. The source, which was operated on argon propellant for the tests, utilized a tungsten filament cathode. The accelerator grid had a single 2.3 cm dia. aperture aligned with the screen grid aperture on the ion source centerline. The grids, which were both 1.5 mm thick, were separated by 2.8 cm.

The test was conducted by operating the ion source over a range of beam currents at various accelerating voltage conditions first without the constraining screen and then with it. At each operating condition the beam current and impingement current were recorded and ion beam was probed using

a Faraday probe located 46 cm downstream of the accel grid. From the Faraday probe data the divergence angle of the beam was computed using the usual definition, namely the half angle of the cone enclosing 95% of the beam current and containing the circumference of the accel grid aperature.

The constraining screen used for this study was made of 0.25 mm dia. tantalum wires separated by $\sim$ 1 mm and arranged in a crossed pattern. It was attached by spot welding it to the upstream screen grid surface. The constraining screen was then deformed mechanically until its position on the hole centerline was 0.03 cm upstream of its original, flat position and its contour appeared to be the same as that for the sheath of a well-focused beamlet.[11]

Results

Results obtained in the tests are presented in Fig. 19 where a comparison of the impingement-to-beam current ratio and the beamlet divergence half angle are shown for various operating conditions both with the constraining screen (open symbols and solid lines) and without it (solid symbols and dashed lines). Normalized perveance per hole (P) values were computed for Fig. 19 using the equation

$$P = \frac{J_B}{V_T^{3/2}} \left[\frac{\ell}{d_s}\right]^2 \qquad (6)$$

where J_B is the beam current, V_T is the total accelerating voltage, and d_s is the screen hole diameter (defined in Fig. 18a). The effective acceleration length ℓ, was assumed to be distance between the accelerator grid plane and an imaginary plane tangent to the constraining screen at the hole centerline. This same distance (ℓ = 3.25 cm) was used to compute the perveance for both the free and constrained sheath results. The net accelerating voltages (V_n) and the net-to-total accelerating voltage ratios (R) given on Fig. 19 can be used to compute the total accelerating voltage needed in Eq. 6.

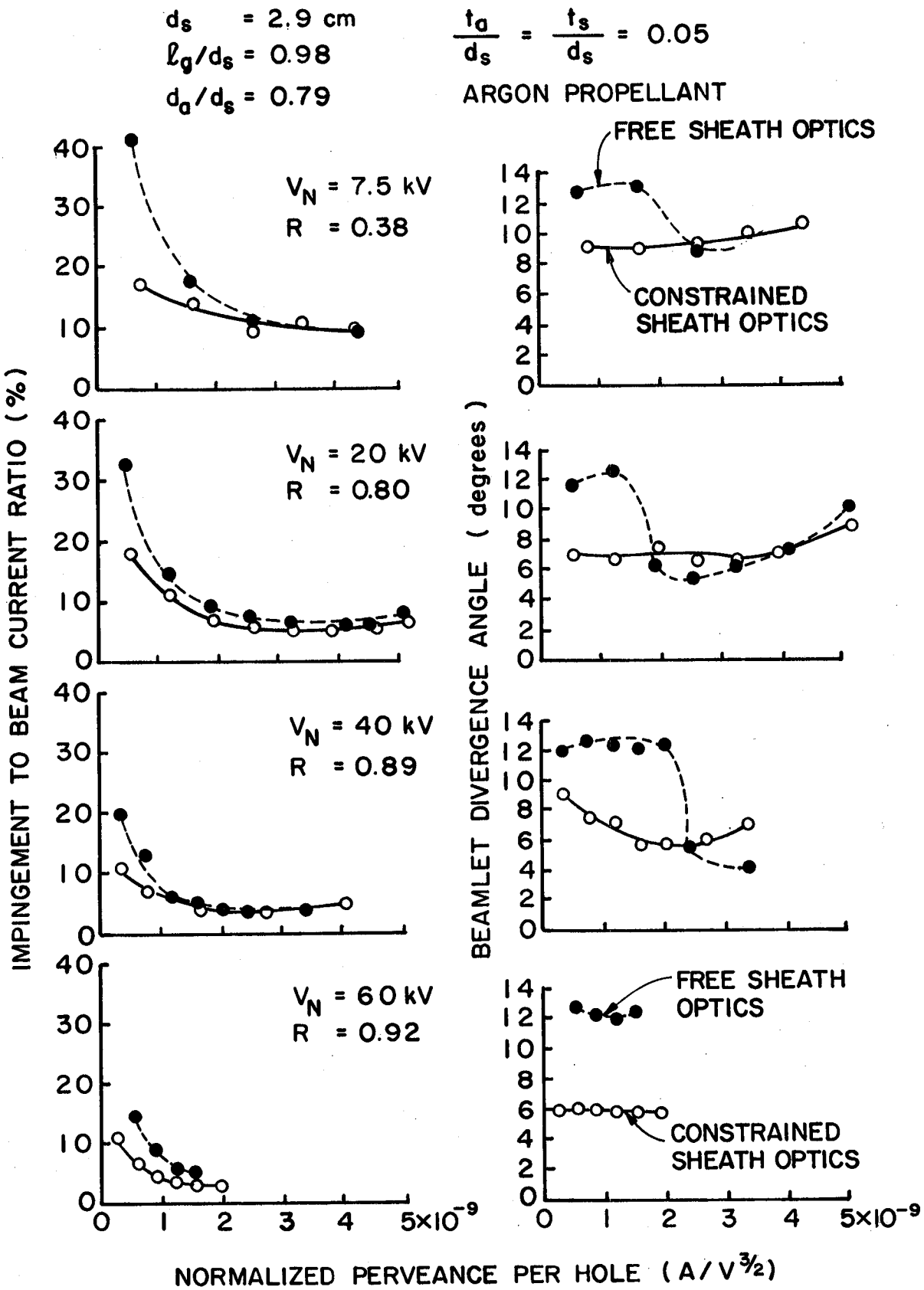

Figure 19. Constrained/Free Sheath Optics Comparison

The data of Fig. 19, which have been collected over a very wide range of net accelerating voltages (7.5 kv to 60 kv), suggest two important points. They are:

1) the impingement currents measured with the constraining screen are either equal to or less than those obtained without it, and
2) the beamlet divergence angles remain relatively constant as either the beam current (i.e. normalized perveance per hole) or the accelerating voltage are changed with the constrained sheath optics while dramatic changes in these angles are observed when the free sheath optics system is used.

It is noted that operation at high perveance levels was not attempted at the higher net accelerating voltage of Fig. 19. Such operation was not attempted because of the fear that the Faraday probe would be destoyed if it were operated in the high energy flux environment that exists in this regime.

Concluding Remarks

It should be noted that the net accelerating voltages used in this study are much higher than those that would be used in typical ion thruster applications. Still, the trends shown support the physical model presented and suggest the constrained sheath optics concept could be used to maintain proper ion beamlet focusing at high beam current densities and low net accelerating voltages without the need for close grid spacings. Such operation would be accomplished by operating at a low net-to-total accelerating voltage ratio. It is also possible that a constrained sheath, single screen grid hole covered with a sheath constraining screen and a single hole accel grid might be used to design an ion optics system. It is noted that considerable additional research needs to be conducted to demonstrate the true potentials of this concept for ion thruster applications. This research should include a study of

the effects of 1) the webbing thickness and spacing and the aperture shapes in the constraining screen, 2) the surface contour of the constraining screen, 3) installation of a third (decel) grid, and 4) operation at the net accelerating voltage and beam current levels appropriate to ion thruster operation.

The following potential advantages of constrained sheath optics over conventional optics are suggested:

- Higher current densities could be achieved at low specific impulses.
- Close grid separations would not be required so grid failures due to thermal distortion and grid shorting by metallic flakes would be much less likely.
- Thrusters having diameters greater than those being tested today could be operated.
- Stable grid system operation could be achieved over a wider range of beam current and acceleration voltage operating conditions.
- The acceleration grid support structure would be simpler to both design and build.

The concept also carries with it some disadvantages relative to conventional designs that should be mentioned. These include:

- The screen grid fabrication requirements could be more complex.
- Discharge chamber performance would be degraded if it were necessary to make the screen grid less transparent to discharge chamber ions than conventional designs.
- The transparency of the grid system to neutral atoms could increase.

Considered in total the potential advantages of the concept are considered sufficient to outweigh the potential disadvantages and the concept is considered sufficiently promising to warrant additional study.

THREE GRID-BEAMLET VECTORING

Barry Andrews

The divergence and deflection characteristics of ion beam optics are important parameters in the design of electrostatic thrusters. At the low net acceleration voltages associated with low specific impulse, inert gas ion thruster operation it becomes necessary to either use an extremely close grid separation distance or to operate at a very low net-to-total accelerating voltage ratio. Operation at a low net-to-total accelerating voltage ratio requires a three grid optics system to assure good optical performance. In order to minimize the off-axis thrust associated with dished grid sets, hole misalignments are used to redirect the emerging beamlets from these three grid systems. A study that would yield either empirical correlations or a theoretical model of beamlet deflection as a function of hole misalignment would facilitate design of these grids. Further, some ion thruster applications would benefit from a beam that could be vectored and grid translation is one method of producing a moderate thrust vectoring capability.[15] In addition, beam focusing may be desirable to increase the current density in such ground-based applications as sputtering.[16] Again a model or empirical correlations describing the effects of hole misalignment on three grid optics would be useful in designing the hardware needed for such equipment. Conrad has proposed a theoretical model of these effects[17] and one purpose of this research is to verify his results over the range of parameters of interest for electric propulsion applications. A second objective is to determine the preferred grid system translation scheme for ion thruster applications.

Apparatus and Procedure

The apparatus and procedures used for this study are identical to those which were used during a previous beamlet vectoring investigation,[2] except for the addition of a decelerator grid and the additional hardware needed to effect its translation. Briefly, a mildly divergent magnetic field 8 cm diameter electron-bombardment ion source is operated on argon propellant. Tungsten wire filaments are used as both the main and neutralizer cathode emitters. The screen, accelerator (accel), and decelerator (decel) grids are made from thin, flat sheet graphite. The grid aperture pattern comprises a nineteen hole hexagonal array with a center-to-center hole spacing of 2.5 mm. Variable grid separation is accomplished by using various numbers of thin mica sheets (0.25 mm thick). The assembled accelerator system is placed on a masked-down discharge chamber, which ensures that the 1 cm^2 hexagonal hole array extracts ions from a near uniform plasma. The decelerator grid is biased 12v below ground potential to prevent neutralization electrons from reaching its surface.

The nomenclature used to describe the geometry of one of the nineteen hole sets in the three grids is shown in Fig. 20. As the figure suggests the apparatus is designed so the accel, decel or both of these grids can be translated to induce beamlet vectoring. The accelerator or decelerator grids can be translated in a direction perpendicular to the grid hole axes during thruster operation by mechanical systems coupled to micrometer assemblies, while the screen grid is held stationary. With this type of arrangement, relative screen grid deflection can also be achieved by translating the accel and decel holes simultaneously in such a way that their axes remain aligned.

A schematic of this grid translating apparatus is shown in Figure 21. Separate assemblies attached to the accel and decel grids are used to translate them under the action of the micrometers, which are located outside of the bell

V_T = TOTAL ACCELERATING VOLTAGE
V_N = NET ACCELERATING VOLTAGE
V_D = DISCHARGE VOLTAGE
R = V_N / V_T

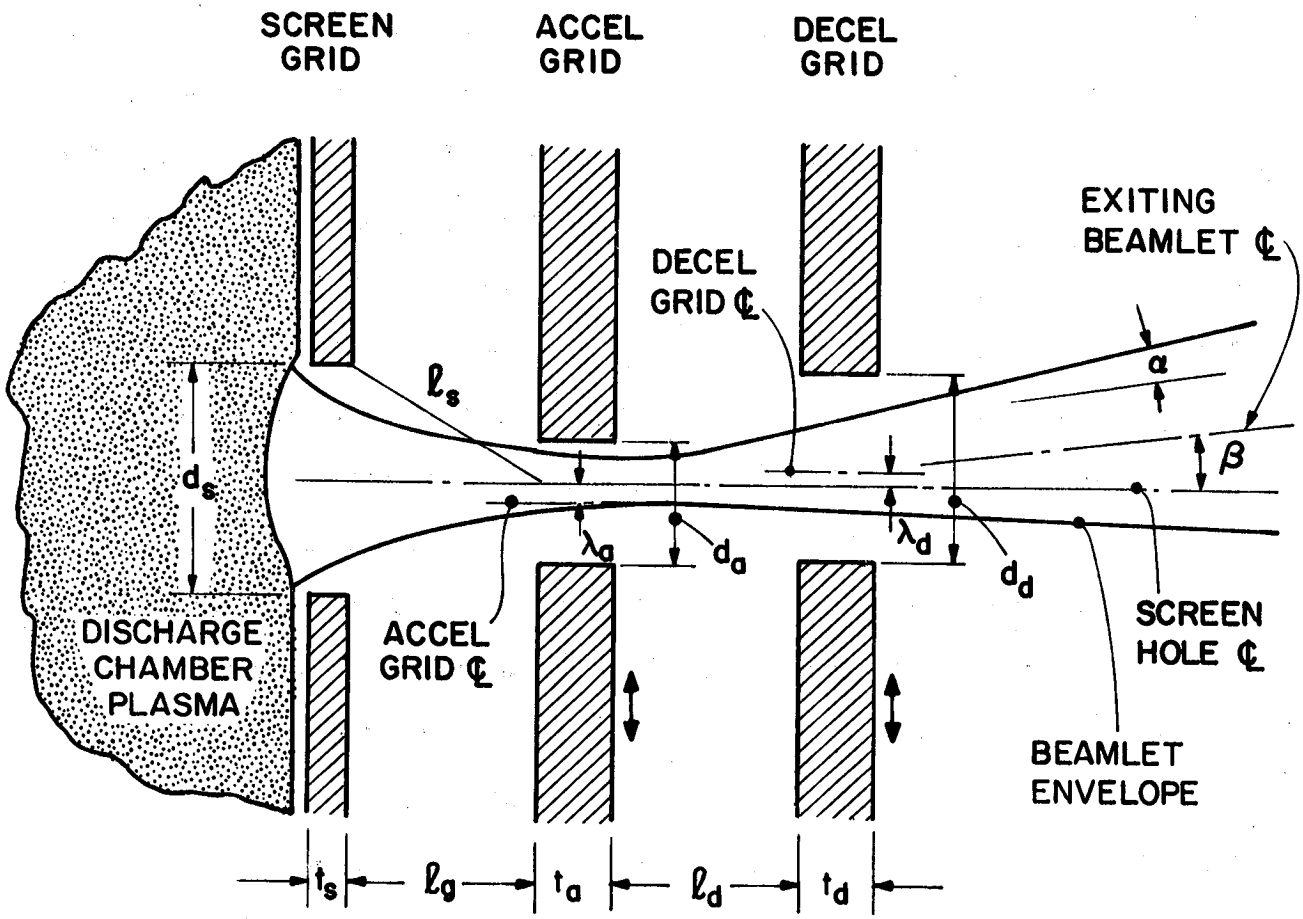

α - BEAM DIVERGENCE ANGLE
β - BEAM DEFLECTION ANGLE
λ_a - ACCEL GRID TRANSLATION
λ_d DECEL GRID TRANSLATION

Figure 20. Three-Grid Deflected Beamlet Nomenclature

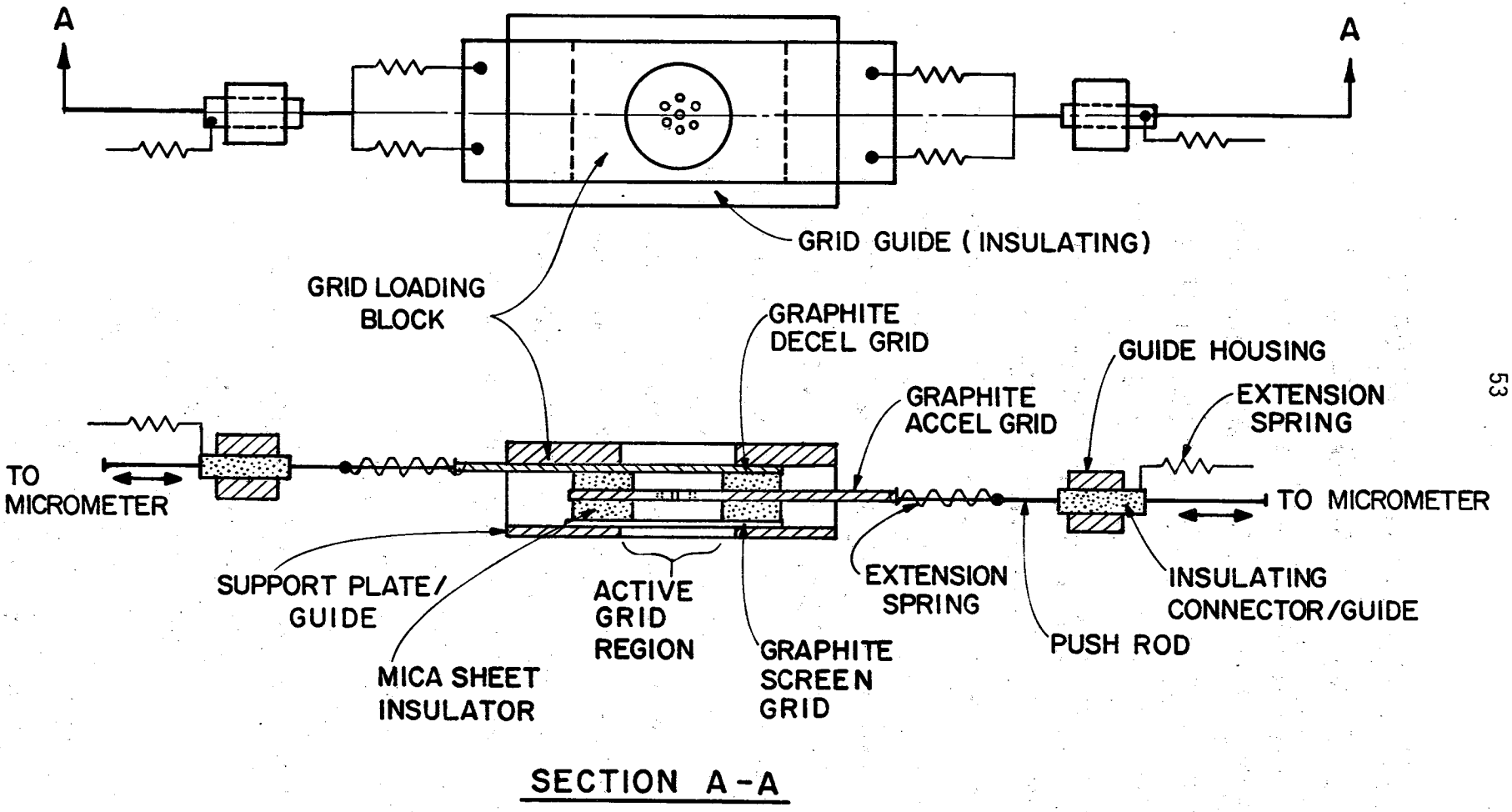

Figure 21. Grid Translation Apparatus

jar. Extension springs are employed to remove the backlash from their assemblies at the push rod/guide interface and at the micrometer/insulating connector-guide interface. The grids are held in place at their sides by grid guides and they are held at the proper spacing by a loading block that compresses the mica spacer/grid sandwich together. Testing of the apparatus has shown it is possible to maintain the desired positioning accurracy (< 0.01 mm) and achieve the needed electrical isolation between the various components of the system that are at different potentials.

The procedure used in this study is similar to that employed by Homa[2] in an earlier experiment. In short, beam current density profiles are measured using a movable probe rake containing thirty individual Faraday ion current sensors which can be positioned at various distances downstream from the accelerator system. The beam current density profiles are recorded and analyzed using a Hewlett Packard 3054 Data Logger in conjunction with a computer routine. A detailed description of how the computer routine calculates divergence and deflection angles can be seen in the aforementioned study by Homa.[2]

For the present study, the standard case selected is defined by the following geometrical and operating conditions:

Screen hole diameter (d_s)	2.06 mm
Total accelerating voltage (V_T)	1100 volts
Discharge voltage (V_D)	40 volts
Net-to-total accelerating voltage ratio (R)	0.70
Screen grid thickness ratio (t_s/d_s)	0.19
Accelerator grid thickness ratio (t_a/d_s)	0.37
Decelerator grid thickness ratio (t_d/d_s)	0.37
Accelerator hole diameter ratio (d_a/d_s)	0.64
Decelerator hole diameter ratio (d_d/d_s)	0.83

Screen-to-accelerator grid separation ratio (ℓ_g/d_s) 0.49

Accelerator-to-decelerator grid separation ratio (ℓ_d/d_s) 0.25

The standard case described above was selected to define a condition at which the performance obtained from this apparatus could be compared to that measured previously in a study of the three inmovable grids.[18]

Results

The data that have been collected so far in this study are considered preliminary. The intent of this study is to determine the preferred way to achieve beamlet steering and then to carry out a parametric study using this preferred method. To this date, the experiments have not yielded sufficiently consistent results so such information as the ratio of deflection angle to grid translation distance can be presented. Research has shown, however, that translation of the accel grid induces beamlet deflection in a direction opposite to accel grid motion while decel or screen grid translation cause the beamlet to be deflected in the same direction as either of these grids is moved. In addition, data collection has consistently shown that the deflection angle is most sensitive to accel grid translation and least sensitive to decel grid translation.

Conclusion

The apparatus needed to test the beamlet deflection induced by translating each of the three grids relative to the other two grids has been developed. Research has indicated that precision grid alignment and stable thruster operation are essential if accurate data are to be obtained. Further work is needed to obtain continuous and consistent values of beamlet deflection as a function grid translation.

APPENDIX A

A Technique for Making Iron Filings Maps in Strong Fields from Permanent Magnets

In order to make magnetic field maps for ring cusp thrusters, 100 mesh iron filings are mixed with a two-component acrylic and the mixture is placed in a thin layer between two slides, made from 1.6 mm thick clear acrylic that fit into the discharge chamber. The acrylic cement nearest the magnets is heated prior to insertion into the discharge chamber to speed curing in these high field strength areas. The slide assembly is then allowed to cool and after several minutes it is placed inside the discharge chamber to cure. The cement in the heated areas near the magnetic field cusps is more viscous than the rest of the mixture and this prevents rapid loss of the iron filings to the edges of the slide in these areas. The un-heated cement is less viscous and this facilitates movement of the iron filings in the lower flux density regions of the source. After the cement has set, the slide may be removed and photocopied. A typical map made in this way is shown in Fig. 4. The time required to make a map is of course dependent on the setting time of the cement being used. Cement having a 1 hour setting time was found to work well in making the map of Fig. 4.

REFERENCES

1. Brophy, John R., "Ion Thruster Performance Model," NASA CR-174810, Dec. 1984.

2. Homa, John M., "Ion Beamlet Steering for Two-grid Electrostatic Thruster," NASA CR-174671, July 1984.

3. Shaw, Ben D., "The Annular Flow Electrothermal Ramjet," NASA CR-174704, July 1984.

4. Sovey, J. S., "Improved Ion Containment Using a Ring-Cusp Ion Thruster," AIAA Paper No. 82-1928, Nov. 1982.

5. Goebel, D. M., "Ion Source Discharge Performance and Stability," The Physics of Fluids, Vol. 25, No. 6., pp. 1093-1103, June 1982.

6. Isaacson, G. G., and Kaufman, H. R., "15-cm Multipole Gas Ion Thruster," Journal of Spacecraft and Rockets, Vol. 14, No. 8, August 1977, pp. 469-473.

7. Rose, D. J. and Clark, Jr., "Plasma and Controlled Fusion," p. 216, M.I.T. press, 1961.

8. deHeer, F. J., et. al., "Total Cross Sections for Electron Scattering by Ne, Ar, Kr and Xe," J. Phys. B: Atom, Molec. Phys., Vol. 12, No. 6, pp. 979-1002, 1979.

9. Beattie, J. R., "Numerical Procedure for Analyzing Langmuir Probe Data," AIAA Journal, Vol. 13, No. 7, pp. 950-952, 1975.

10. Siegfried, D. S., "Xenon and Argon Hollow Cathode Research," appears in NASA CR-168340, P. J. Wilbur, ed., Jan. 1984, pp. 76-132.

11. Aston, G. and P. J. Wilbur, "Ion Extraction from a Plasma," J. Appl. Phys., V. 52, No. 4, April 1981.

12. Brewer, G. R., Ion Propulsion, pp. 185-197, Gordon and Breach, New York 1970.

13. Byers, David C., "An Experimental Investigation of a High-Voltage Electron-Bombardment Ion Thruster," J. of Electrochem Soc., V. 116, No. 1, Jan. 1969, pp. 9-17.

14. Aston, G. and W. D. Deininger, "Test Bed Ion Engine Development," NASA CR-174623, March 1984.

15. Latham, W. C. and W. B. Adam, "Theoretical Analysis of a Grid Translation Beam Deflection System for a 30 cm Diameter Kaufman Thruster," NASA TM X-67911, 1971.

16. Kaufman, H. R., J. M. E. Harper, and J. J. Cuomo, "Focused Ion Beam Design for Sputter Deposition," Journal of Vac. Science & Tech., May/June 1979, pp. 899-905.

17. Conrad, J. R., "Beamlet Steering by Aperture Displacement in Ion Sources with Large Acceleration-Deceleration Ratio," Rev. Sci. Inst. v. 51, April 1980, pp. 418-424.

18. Aston, G. and Kaufman, H. R., "Ion Beam Divergence Characteristics of Three-Grid Accelerator Systems," AIAA Journal, Vol. 17, Jan. 1979, pp. 64-70.

DISTRIBUTION LIST

	Copies
National Aeronautics and Space Administration Washington, DC 20546	
Attn: E/Mr. Earle Vanlaningham MS B607	1
A/Mr. Bob Wasal, MS B600	1
National Aeronautics and Space Administration Lewis Research Center 21000 Brookpark Road Cleveland, OH 44135	
Attn: Aerospace Technology Section	
Mr. Bob Firestone, MS 500-305	1
Technology Utilization Office, MS 7-3	1
Report Control Office, MS 60-1	1
Library, MS 60-3	2
Mr. N. Musial, MS 500-113	1
Dr. M. Goldstein, Chief Scientist, MS 5-9	1
Mr. Dave Byers, MS 500-219	1
Mr. Frank Berkopec, MS 500-219	1
Mr. Jim Stone, MS 500-219	1
Mr. Vince Rawlin, MS500-219	20
Mr. Bruce Banks, MS77-4	1
National Aeronautics and Space Administration Lyndon B. Johnson Space Center Houston, TX 77058	
Attn: Mr. Hu Davis	1
National Aeronautics and Space Administration Marshall Space Flight Center Huntsville, AL 35812	
Attn: Mr. Robert Bechtel	1
Research and Technology Division Wright-Patterson AFB, OH 45433	
Attn: (ADTN) Mr. Everett Bailey	1
NASA Scientific and Technical Information Facility P. O. Box 8757 Baltimore, MD 21240	
Attn: Accessioning Dept.	1
Dept. of the Navy Office of Naval Research University of New Mexico Bandelier Hall West Albuquerque, NM 87131	
Attn: G. Max Irving	1

	Copies
Case Western Reserve University 10900 Euclid Avenue Cleveland, OH 44106 Attn: Dr. Eli Reshotko	1
DST 1 Ministry of Defence Metropole Building Northumberland Avenue London, WC2 N5BL ENGLAND Attn: Dr. D. G. Fearn	1
United Kingdom Atomic Energy Authority Culham Laboratory Abingdon, Berkshire ENGLAND Attn: Dr. P. J. Harbour Dr. M. F. A. Harrison	1 1
National Aeronautics and Space Administration Goddard Space Flight Center Greenbelt, MD 20771 Attn: Mr. A. A. Vetman Dr. David H. Suddeth	1 1
COMSAT Laboratories P. O. Box 115 Clarksburg, MD 20734 Attn: Mr. B. Free Mr. O. Revesz	1 1
Comsat Corporation 950 L'Enfant Plaza, SW Washington, DC 20024 Attn: Mr. Sidney O. Metzger	1
Intelsat 490 L'Enfant Plaza, S.W. Washington, DC 20024 Attn: Mr. Rolland Schreib	1
Rocket Propulsion Laboratory Edwards AFB, CA 93523 Attn: LKDH/Dr. Robert Vondra LKDH/Lt. Phil Roberts, MS 24	1 1
DFVLR - Institute fur Plasmadynamik Technische Universitat Stuttgart 7 Stuttgart-Vaihingen Allmandstr 124 West Germany Attn: Dr. Gerhard Krulle	1

	Copies
Giessen University 1st Institute of Physics Giessen, West Germany Attn: Professor N. W. Loeb	1
Jet Propulsion Laboratory 4800 Oak Grove Laboratory Pasadena, California 91102 Attn: Technical Library	1
Mr. James Graf	1
Dr. Graeme Aston	1
Dr. Dennis Fitzgerald	1
Dr. John Brophy	1
Electro-Optical Systems, Inc. 300 North Halstead Pasadena, California 91107 Attn: Mr. E. James	1
Mr. W. Ramsey	1
TRW Inc. TRW Systems One Space Park Redondo Beach, California 90278 Attn: Mr. Sid Zafran	1
National Aeronautics and Space Administration Ames Research Center Moffett Field, California 94035 Attn: Technical Library	1
National Aeronautics and Space Administration Langley Research Center Langley Field Station Hampton, Virginia 23365 Attn: Technical Library	1
Hughes Research Laboratories 3011 Malibu Canyon Road Malibu, California 90265 Attn: Mr. J. H. Molitor	1
Dr. R. L. Poeschel, MS RL 57	1
Dr. Jay Hyman, MS RL 57	1
Dr. J. R. Beattie	1
Dr. W. S. Williamson	1
Dr. H. J. King	1
Princeton University Princeton, NJ 08540 Attn: Dean R. G. Jahn	1
Dr. Arnold Kelly	1

	Copies
Boeing Aerospace Co. P. O. Box 3999 Seattle, Washington 98124 Attn: Mr. Donald Grim, MS 8K31	1
Lockheed Missiles and Space Co. Sunnyvale, California 94088 Attn: Dr. William L. Owens Dept. 57-24	1
Electrotechnical Laboratory 1-1-4, Umezono, Sakura-Mura, Niihari-Gun Ibaraki, Japan Attn: Dr. Katsuya Nakayama	1
Sandia Laboratories Mail Code 4537 Albuquerque, NM 87115 Attn: Mr. Ralph R. Peters Mr. Dean Rovang	1 1
Ion Tech Inc. 2330 E. Prospect Road Fort Collins, Colorado 80525 Attn: Dr. Gerald C. Isaacson Dr. Dan Siegfried	1 1
EG & G Idaho P. O. Box 1625 Idaho Falls, Idaho 83401 Attn: Dr. G. R. Longhurst, TSA-104	1
Michigan State University East Lansing, MI 48824 Attn: Dr. J. Asmussen Dr. M. C. Hawley	1 1
The Takagi Research Laboratory Department of Electronics Kyoto University Yoshidahonmachi Sakyo-ku Kyoto 606 JAPAN Attn: Dr. Toshinori Takagi	1
Department of Aeronautics Faculty of Engineering University of Tokyo 7-3-1, Hongo, Bunkyo-ku Tokyo, JAPAN Attn: Prof. Itsuro Kimura	1

	Copies
Prof. Tom Maul P. O. Box 98182 Tsim Sha Tsui Post Office Kowloon, Hong Kong British Crown Colony	1
Mr. Susumu Masaki Department of Electronics Tokyo National Technical College No. 1220-2 Kunugida-cha, Hachioji 193 Tokyo, JAPAN	1
Dr. Pradosh Ray Tuskegee Institute School of Engineering Tuskegee Institute, Ala. 36088	1
Dr. John Barber International Applied Physics Inc. 7546 McEwen Road Dayton, Ohio 45459	1
Dr. M. Krishnan Dept. of Applied Physics P. O. Box 2159 Yale Station New Haven, Connecticut 06520	1
Mr. Lee W. Parker 252 Lexington Road Concord, Massachusetts 01742	1
Dr. Chris Olson Dept. of Physics University of Huntsville Huntsville, AL 35899	1
Dr. Kevin Rudolph MS M0482 Martin Marietta Aerospace P.O. Box 179 Denver, Colorado 80201	1
Dr. Rolf Buhler Institut fur Raumfahrtantriebe Universitat Stuttgart 7 Stuttgart 80 Pfaftenwaldring 31 West Germany	1
Internal Distribution: Dr. R. S. Robinson	1

	Copies
Dr. Ira Katz Systems, Science and Software P. O. Box 1620 LaJolla, CA 92038	1
Dr. David Finkelstein Physics Department Georgia Institute of Technology Atlanta, GA 30332	1
Dr. Rod Burton G-T Devices, Inc. 5705 A General Washington Dr. Alexandria, VA 22312	1
Instituto de Pesquisas Espaciais - INPE Library and Documentation Division C.P. 515 Sao Jose dos Campos - SP 12200 - Brazil	1
Dr. Herb Cohen/LKB Air Force Geophysics Laboratory Hanscom, AFB, Mass. 01731	1
Dr. Chuck Crawford Kimball Physics Inc. Kimball Hill Road Wilton, N.H. 03086	1
Dr. Roy Clampitt Crawley Mill, Witney Oxfordshire OX8 5TJ ENGLAND	1